Sensor-Independent LAI/FPAR CDR: Reconstructing a Global Sensor-Independent Climate Data Record of MODIS and VIIRS LAI/FPAR from 2000 to 2022

Jiabin Pu[1], Kai Yan[2], Samapriya Roy[3], Zaichun Zhu[4], Miina Rautiainen[5], Yuri Knyazikhin[1], Ranga B. Myneni[1]

[1]Department of Earth and Environment, Boston University, Boston, MA 02215, USA
[2]Faculty of Geographical Science, Beijing Normal University, Beijing, 100875, China
[3]University of Arizona, Tucson, AZ 85721, USA
[4]School of Urban Planning and Design, Shenzhen Graduate School, Peking University, Shenzhen 518055, China
[5]Aalto University, School of Engineering, P.O. Box 14100, FI-00076 Aalto, Finland

Correspondence to: Kai Yan (kaiyan@bnu.edu.cn)

Abstract. Leaf area index (LAI) and fraction of photosynthetically active radiation (FPAR) are critical biophysical parameters for the characterization of terrestrial ecosystems. Long-term global LAI/FPAR products, such as MODIS&VIIRS, provide the fundamental dataset for accessing vegetation dynamics and studying climate change. However, existing global LAI/FPAR products suffer from several limitations, including spatial-temporal inconsistencies and accuracy issues. Considering these limitations, this study develops a Sensor-Independent (SI) LAI/FPAR climate data record (CDR) based on Terra-MODIS/Aqua-MODIS/VIIRS LAI/FPAR standard products. The SI LAI/FPAR CDR covers the period from 2000 to 2022, at spatial resolutions of 500m/5km/0.05 degrees, 8-day/bimonthly temporal frequencies and available in sinusoidal and WGS1984 projections. The methodology includes (*i*) comprehensive analyses of sensor specific quality assessment variables to select high quality retrievals, (*ii*) application of the spatial-temporal tensor (ST-Tensor) completion model to extrapolate LAI and FPAR beyond areas with high quality retrievals, (*iii*) generation of SI LAI/FPAR CDR in various projections, spatial and temporal resolutions, and (*iv*) evaluation of the CDR by direct comparisons to ground data and indirectly through reproducing results of LAI/FPAR trends documented in literature. This paper provides a comprehensive analysis of each step involved in the generation of the SI LAI/FPAR CDR, as well as evaluation of the ST-Tensor completion model. Comparisons of SI LAI (FPAR) CDR with ground truth data suggest a RMSE of 0.84 LAI (0.15 FPAR) units with R^2 of 0.72 (0.79), which outperform the standard Terra/Aqua/VIIRS LAI (FPAR) products. The SI LAI/FPAR CDR is characterized by a low time series stability (TSS) value, suggesting a more stable and less noisy data set than sensor-dependent counterparts. Furthermore, the mean absolute error (MAE) of the CDR is also lower, suggesting that SI LAI/FPAR CDR is comparable in accuracy with high-quality retrievals. LAI/FPAR trend analyses based on the SI LAI/FPAR CDR agrees with previous studies, which indirectly provides enhanced capabilities to utilize this CDR for studying vegetation dynamics and climate change. Overall, the integration of multiple satellite data sources and the use of advanced gap-filling modelling techniques improve the accuracy of the SI LAI/FPAR CDR, ensuring the reliability of long-term vegetation studies, global carbon cycle modelling, and land

policy development for informed decision-making and sustainable environmental management. The SI LAI/FPAR CDR is open access and available under a Creative Commons Attribution 4.0 License at https://doi.org/10.5281/zenodo.8076540 (Pu et al., 2023a).

Keywords: MODIS, VIIRS, LAI, FPAR, Sensor-Independent, CDR.

1 Introduction

The leaf area index (LAI) is a fundamental parameter for quantifying the structural and functional characteristics of terrestrial vegetation canopies, defined as half of the total green foliage per unit of horizontal ground area (Chen and Black, 1992;Chen, 1996). LAI plays an essential role in models of ecological processes, global primary productivity, climate dynamics, water cycle and the carbon cycle analysis (Sellers et al., 1997;Boussetta et al., 2013;Piao et al., 2015;Fang et al., 2019;Chen et al., 2022). The fraction of incident photosynthetically active radiation (400-700 nm) absorbed by vegetation (FPAR) is an important biophysical parameter used to quantify the energy absorption capacity of the vegetation canopy (Knyazikhin et al., 1998a;Myneni et al., 2002). LAI and FPAR are key climate variables and biodiversity metrics identified by the United Nations Global Climate Observing System (GCOS)(Skidmore et al., 2015).

In recent decades, there has been a remarkable increase in the use of global long-term satellite-derived LAI/FPAR datasets from various sensors, e.g., the Advanced Very High-Resolution Radiometer (AVHRR), the Moderate Resolution Imaging Spectroradiometer (MODIS), and the Visible Infrared Imager Radiometer Suite (VIIRS). Among these, the LAI/FPAR products from MODIS on the Terra platform have been widely used since 2000 and represent a milestone in operational generation of vegetation parameters from satellite observations (Knyazikhin, 1999;Myneni and Park, 2015;Yan et al., 2016;Yan et al., 2021c). The LAI/FPAR are also available from MODIS on the Aqua platform and VIIRS on the Suomi National Polar-Orbiting Partnership (S-NPP) and the Joint Polar Satellite System (JPSS) satellites since 2002 (2012), ensuring the extension of the Terra MODIS long-term data record (Justice et al., 2013). The MODIS&VIIRS LAI/FPAR datasets have contributed significantly to many studies, such as terrestrial carbon sinks, understanding seasonal and interannual variations in equatorial forests, analyses of spatial patterns of drought, and climate and energy flux dynamics (Tang et al., 2013;Mariano et al., 2018;Chen et al., 2019;Chen et al., 2022;Sun et al., 2022).

Two weaknesses of the MODIS/VIIRS LAI/FPAR products have been identified (i.e., temporal stability and absolute accuracy), which limit their application in vegetation dynamic studies (Fang et al., 2012a;Fang et al., 2019;Yan et al., 2021a). These problems mainly arise due to uncertainties in input information to the operational retrieval algorithm such as surface reflectance and land cover type (Knyazikhin, 1999;Fang et al., 2019;Tian et al., 2000). Several post-processing techniques have been proposed to remove uncertainties in the MODIS&VIIRS LAI/FPAR standard products. These include 1) identifying areas with a high fraction of water area in the satellite pixel and removing their impact on the retrieval using a mixed pixel correction method (Xu et al., 2020;Dong et al., 2023); 2) integration of prior knowledge of reflectance variations into the generation of the image composite (Pu et al., 2023b); 3) accounting for the canopy hot spot effect in the retrieval technique

65 (Yan et al., 2021b). These methods would increase product spatial coverage. And the scientific community also developed various gap filling techniques to extrapolate retrievals beyond areas with valid satellite observations such as 1) cubic splines (Mitášová and Hofierka, 1993); 2) spatial linear, bilinear and kriging interpolations (Xu et al., 2015;Smith, 1981;Oliver and Webster, 1990), 3) various temporal extrapolation techniques (Holben, 1986;Lange et al., 2017;Roerink et al., 2000;Zhu et al., 2011;Das and Ghosh, 2017;Chu et al., 2021;Wang et al., 2023). However, most of the approaches are characterized by high

70 computational costs or lack of information necessary for their implementation at the global scale. Consequently, most research has been limited to specific regions (e.g., China and North America), leaving a significant gap in developing Climate Data Record (CDR). Which by definition is a consistently-processed time series of uncertainty-quantified data, located in time and space, of sufficient length and quality to be useful for climate time-scale uses (Merchant et al., 2017).

   The objective of this paper is to develop a long-term LAI and FPAR CDR using standard LAI and FPAR products from

75 MODIS and VIIRS sensors. Our approach includes (*i*) comprehensive analyses of sensor-specific quality assessment (QA) variables to select high-quality retrievals, (*ii*) application of the spatial-temporal tensor (ST-Tensor) completion model (Chu et al., 2021) to extrapolate LAI and FPAR beyond areas with high quality retrievals, (*iii*) generation of SI LAI/FPAR CDR in various projections, spatial and temporal resolutions, and (*iv*) evaluation of the CDR by direct comparisons to ground measurement and indirectly through reproducing results of LAI/FPAR trend analyses to revisit the Greening Earth.

80   The paper is organized as follows. Section 2 introduces the data used in this study and the study area. Section 3 details the steps involved in generating the SI LAI/FPAR CDR, including analyses of sensor-specific QA, generation of high-quality Filtered SI LAI/FPAR timeseries, and applying ST-Tensor completion model. The results of the validation and evaluation are presented in Section 4. Section 5 discusses the underlying factors that contributed to the improvement of the SI LAI/FPAR CDR and the associated issues and challenges. The final section concludes the paper by summarizing the key findings and

85 highlighting the significance of the research.

2 Datasets and Study Area

2.1 LAI/FPAR Products: MOD15A2H, MYD15A2H, and VNP15A2H

   The MODIS&VIIRS LAI/FPAR inputs surface bidirectional reflectance factors (BRFs) in the red and near-infrared (NIR) spectral bands, their uncertainties, sun-sensor geometry, and biome classification map and retrieves the LAI and FPAR for

90 each satellite pixel. The retrieval technique consists of a main algorithm which is based on the radiative transfer equation (RTE) and a backup algorithm, which uses empirical relationships between normalized difference vegetation index (NDVI) and canopy LAI/FPAR (Myneni et al., 2002;Yan et al., 2018;Knyazikhin, 1999;Knyazikhin et al., 1998b). The main algorithm compares the observed spectral BRF with those evaluated from the RTE-based entries stored in a look-up-table (LUT) for a suite of canopy structures and soil patterns that represent an expected range of typical conditions for a given biome type. All

95 canopy/soil patterns for which modelled and observed BRFs differ within a specified uncertainty level are considered as

acceptable solutions. The mean values of LAI and FPAR and their dispersions are reported as retrievals and their uncertainties. When this method fails to localize a solution, the backup method is utilized (Myneni et al., 2002;Yan et al., 2018).

Analyses of the performance of the MODIS LAI/FPAR algorithm indicate that the best quality, high-precision retrievals are obtained from the main algorithm. In the case of dense canopies, the BRFs saturate and become weakly sensitive to changes in canopy properties. The reliability of parameters retrieved under the condition of saturation is lower than that generated by the main algorithm using unsaturated BRF. The algorithm path is the key quality assessment (QA) flag that provides information about the overall quality of the LAI/FPAR. It includes four values (from highest to lowest quality): the main algorithm without saturation, the main algorithm with saturation, the backup algorithm due to sun-sensor geometry, and the backup algorithm due to other reasons. The QA variables provide information about the cloud state, aerosol load, and the presence of snow, which are inherited from the upstream BRF product (Knyazikhin, 1999;Myneni and Park, 2015;Yan et al., 2016;Park et al., 2017).

The daily retrievals are composited over an 8-day period by selecting the LAI and FPAR pair corresponding to the maximum FPAR value generated by the main algorithm (Knyazikhin and Myneni, 2018). The backup algorithm retrievals are selected only when no main algorithm retrievals are available during the 8-day compositing period. The 8-day composited LAI/FPAR product is distributed to the public from the NASA EOSDIS Land Processes Distributed Active Archive Center (Myneni et al., 2015;Myneni and Knyazikhin, 2018).

In this study, we used the Collection 6 (C6) MOD15A2H, C6 MYD15A2H, and the Collection 1 (C1) VNP15A2H LAI/FPAR products. The products are available at 500m sinusoidal grid and are updated every 8 days, resulting in approximately 46 composites per year. MOD15A2H data have been available since 18 February 2000, MYD15A2H since 14 July 2002 and VNP15A2H since 17 January 2012. These datasets are distributed in standard hierarchical data format (HDF) files. Each HDF file contains six scientific data sets (SDS): FPAR, LAI, FparLai_QC, FparExtra_QC, FparStdDev, and LaiStdDev. The LAI and FPAR layers contain the LAI/FPAR retrievals, while the FparLai_QC and FparExtra_QC layers provide information about the algorithm paths and atmospheric conditions. This quality information underlies the first step in generating SI LAI/FPAR CDR, as detailed in Section 3.1.

2.2 Land Cover Map: MCD12Q1

The MODIS land cover product (MCD12Q1) provides a global map of land cover types at a spatial resolution of 500 meters and an annual time step (Sulla-Menashe and Friedl, 2018). In this study, we used the LAI legacy classification scheme (LC_Type_3), which categorizes global vegetation into eight biomes: grasses and cereal crops (Biome 1), shrubs (Biome 2), broadleaf crops (Biome 3), savannas (Biome 4), Evergreen Broadleaf Forests (EBF, Biome 5), Deciduous Broadleaf Forests (DBF, Biome 6), Evergreen Needleleaf Forests (ENF, Biome 7), and Deciduous Needleleaf Forests (DNF, Biome 8) (Sulla-Menashe and Friedl, 2018). The biome classification map is an important auxiliary dataset for MODIS&VIIRS LAI/FPAR operational algorithms. It reduces the number of unknowns of the inverse problem through the use of simplifying assumptions

(e.g., leaf normal orientation) and standard constants (e.g., leaf albedo, patterns of ground reflectance) that are assumed to vary with the biome (Knyazikhin, 1999). A global distribution of 8 biomes is shown in Fig. 1.

2.3 Ground LAI/FPAR Reference

The growing utilization of Earth observation (EO) products has highlighted the importance of addressing product uncertainty through validation based on ground measurements (Baret et al., 2006;Yang et al., 2006;Fang et al., 2012b). In our study, we validated the SI LAI/FPAR CDR by comparing their values with LAI and FPAR ground reference data from version 3 Copernicus Ground-Based Observations for Validation (GBOV) and version 2 DIRECT database (Brown et al., 2020;Brown et al., 2021). The combined utilization of both sets of measured data provides comprehensive coverage across the globe, encompassing a diverse array of representative biome types. The only notable exceptions are the eastern part of China and Eastern Europe, which lacks the measurement sites.

GBOV, part of the Copernicus Global Land Service, aims to facilitate the use of ground-based observations to validate EO products and ensure their quality and consistency. GBOV collects multi-year ground-based observations from global networks and upgrades existing sites or establishes new ones to bridge thematic or geographic gaps (Brown et al., 2020;Bai et al., 2022). To ensure data quality, the GBOV reference database has undergone rigorous quality control procedures and includes various measurements such as top of canopy reflectance, surface albedo, LAI, FPAR, proportion of ground cover, soil moisture at 5 cm depth, and surface temperature. GBOV data are available through the open GBOV portal (https://gbov.acri.fr). We used the GBOV LAI/FPAR maps since 2014 as a reference dataset. We selected 29 GBOV sites of 3 km x 3 km each (see Fig. 1). The LAI/FPAR reference maps were averaged over the 3 km x 3 km area for product assessment. Statistics based on downloaded data, the GBOV validation data set used in this study consisted of 9805 LAI and 10548 FPAR measurements.

The DIRECT LAI, FPAR, and vegetation cover are available as spatially-average values over 3km x 3km reference maps (Brown et al., 2021). Following the CEOS WGCV LPV good practice, the ground data are enhanced with high spatial resolution imagery to account for spatial heterogeneity. This dataset includes 176 global sites representing 7 major biome types, covering the period from 2000 to 2021. Forest sites without understorey are filtered out of the DIRECT database (https://calvalportal.ceos.org/lpv-direct-v2.1). The dataset used in this study contains 446 LAI and 109 FPAR measurements.

2.4 Study Area

Fig. 1 shows distribution of biome types and selected GBOV and DIRECT validation sites. We selected a study area of global, and selected the typical area of 86°W to 30°W and from 20°S to 10°N (zoom-in case in Fig. 1), containing Amazonian forests to highlight the importance of various steps in developing the SI LAI/FPAR CDR. Obtaining high-quality observations over this area is difficult due to a large amount of cloud-contaminated data. It is therefore particularly valuable to assess the quality of our LAI/FPAR CDR in this region.
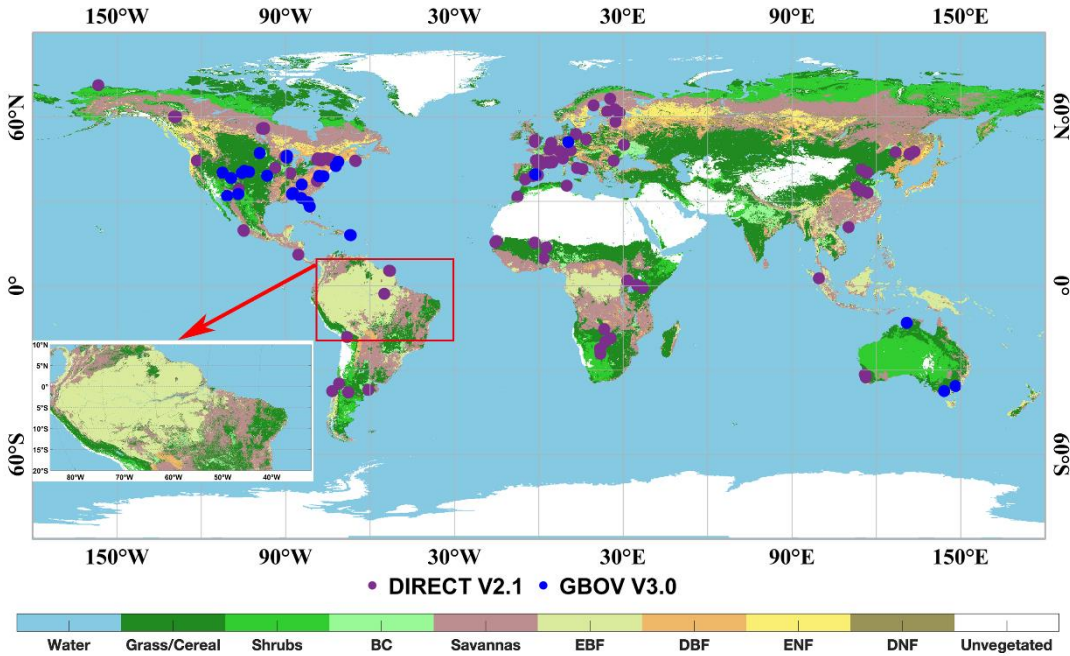
Figure 1. Distribution of the selected GBOV and DIRECT sites. Amazonian forests used as a study area to assess various steps in developing LAI/FPAR CDR is shown as a red square. The background color indicates the biome types from the MCD12Q1 classification schemes of the year 2017 (grasses and cereal crops (Biome 1), shrubs (Biome 2), broadleaf crops (Biome 3), savannas (Biome 4), Evergreen Broadleaf Forests (EBF, Biome 5), Deciduous Broadleaf Forests (DBF, Biome 6), Evergreen Needleleaf Forests (ENF, Biome 7), and Deciduous Needleleaf Forests (DNF, Biome 8)). The blue and purple dots represent the GBOV3.0 and DIRECT2.1 sites.

2.5 Metrics for Evaluating

In this study, we assessed the variability of SI LAI/FPAR CDR using two metrics: time series stability (TSS) (Weiss et al., 2007;Zou et al., 2022) and mean absolute error (MAE) (Zhou et al., 2015). Both metrics provide insight into the uncertainties associated with a dataset. TSS quantifies the deviation of a value at a given time (t_0) from the linear interpolation line calculated from the preceding and succeeding time series data points (Eq. 1).

$$\text{TSS}(t_0) = \frac{|(X(t_1)-X(t_{-1}))\times t_0-(t_1-t_{-1})\times X(t_0)-(X(t_1)-X(t_{-1}))\times t_{-1}+(t_1-t_{-1})\times X(t_{-1})|}{\sqrt{(X(t_1)-X(t_{-1}))^2+(t_1-t_{-1})^2}} \tag{1}$$

We analysed three adjacent time series data points, $X(t_1)$, $X(t_0)$, and $X(t_{-1})$, obtained at the following (t_1), current (t_0), and the previous (t_{-1}) times, respectively. To ensure a fair comparison, we calculated the cumulative TSS based on the same length of time series. The TSS represents the deviation of a value at a given point in time from the linear interpolation line, and in this study, higher TSS values indicate greater variability over time.

The MAE metric is employed in this study to evaluate the accuracy of the retrieval methods by measuring the average absolute difference between the predicted and actual values. Following the approach proposed by (Zhou et al., 2015), the MAE is calculated as the discrepancy between the reference and the retrieved series. We used the MAE as a metric to assess the similarity (Eq (2)). The process of generating the reference time series will be discussed in Section 3.2.

$$MAE = \sqrt[2]{\frac{\sum_{i=1}^{N}(retrieved(i)-reference(i))^2}{N}} \tag{2}$$

Furthermore, performance analyses indicate that the retrievals from the main algorithm without clouds and aerosols provide the highest quality and accuracy (Pu et al., 2020). Therefore, we used a retrieval index (RI), which represents the percentage of pixels with high-quality retrievals (Xu et al., 2018;Yan et al., 2018;Yan et al., 2021a), as an indicator of the uncertainty of the LAI/FPAR retrievals (Eq. 3). This *RI* serves as an additional measure to assess the uncertainty associated with LAI/FPAR retrievals.

$$RI = \frac{Number\ of\ high-quality\ pixels}{Number\ of\ all\ pixels} \tag{3}$$

2.6 Calculation of LAI/FPAR trends

Trends in annual average SI LAI/FPAR CDR (2001 to 2022) are evaluated by the Mann–Kendall (MK) test. The MK test is a non-parametric statistical test commonly used for climate diagnostics and prediction. It enables the detection of monotonic trends in time series data, helping to determine if significant trends exist (Hamed and Rao, 1998). The MK test is employed as follows:

$$S = \sum_{i=1}^{n-1}\sum_{j=i+1}^{n} sgn(x_j - x_i) \tag{4}$$

$$Var(S) = \frac{n(n-1)(2n+5)-\sum_{i=1}^{m}t_i(t_i-1)(2t_i+5)}{18} \tag{5}$$

$$Z_s = \begin{cases} \frac{S-1}{\sqrt{Var(S)}}, & \text{if } S > 0 \\ 0, & \text{if } S = 0 \\ \frac{S+1}{\sqrt{Var(S)}}, & \text{if } S < 0 \end{cases} \tag{6}$$

Equation 4 calculates the sum (*S*) of step function values, which represent the differences between values at different points (x_j and x_i) in the time series. The function sgn(x) takes the value 1 if its argument is a positive number, and -1 otherwise. The variables *n* and *m* denote the number of data points and the number of tied groups (recurring data sets), respectively. Next in Equation 5, the variance (*Var(S)*) is calculated by assessing the magnitude of *S* to evaluate the statistical significance of the detected trends. Where the t_i is the number of the ties (the number of repeats in the extent *i*). Finally, we calculated the test statistic Z_s (Equation 6). When $|Z_s| > Z_{1-\alpha/2}$, the null hypothesis (i.e., no trend) is rejected and the α is a special significance level. Here, we use the significance level of $\alpha = 0.05$ and the $Z_{1-\alpha/2} = 1.96$. Thus, the trends with $P \leq 0.05$ are considered to be statistically significant in this study.

3 Methodology
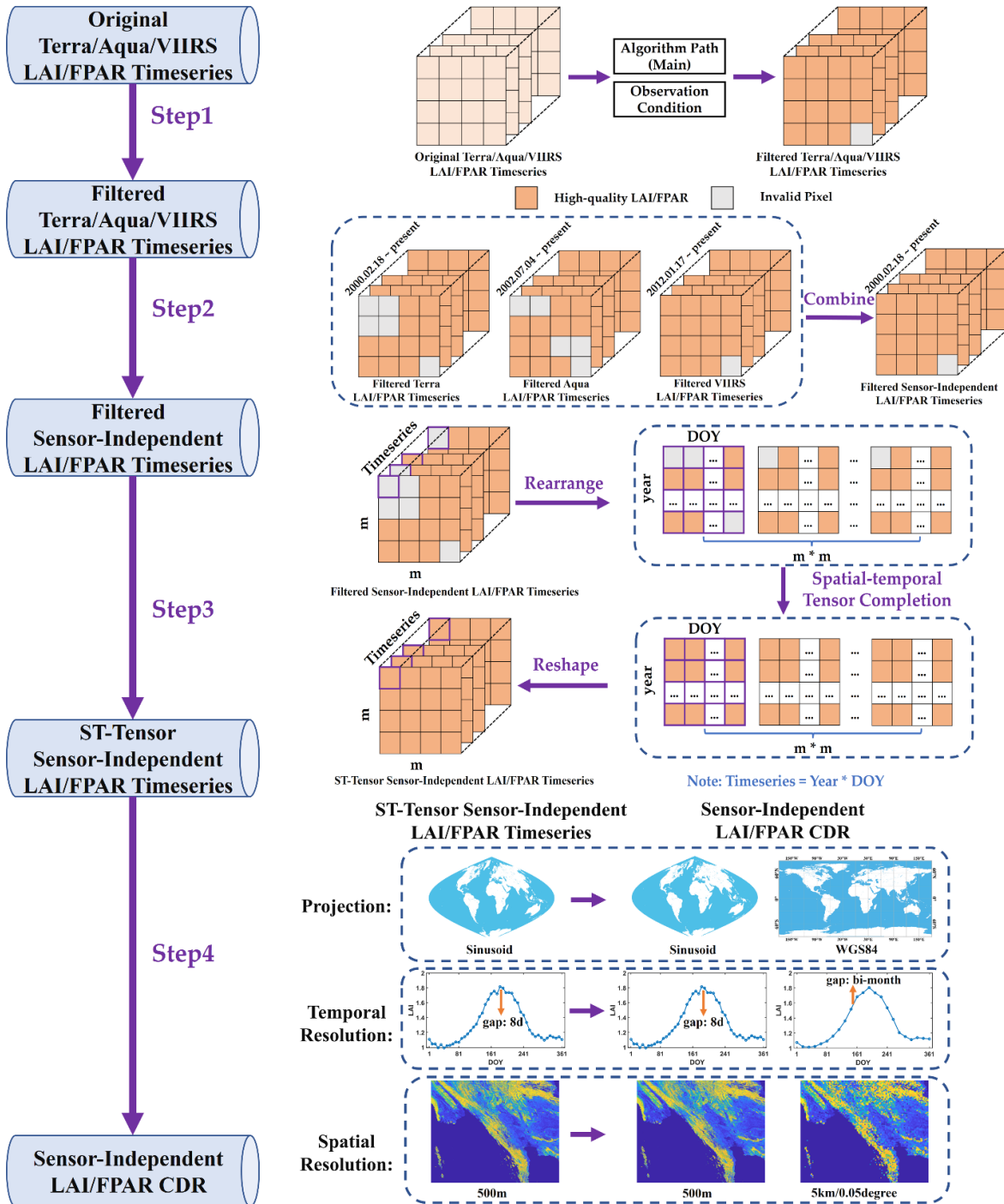
Figure 2. Schematic flowchart of the generation of the SI LAI/FPAR CDR.

205   Our methodology includes four key steps as shown in Fig. 2: 1) Filtering low-quality observations based on QA values; 2) Consolidating the Filtered Terra/Aqua/VIIRS LAI/FPAR into Filtered SI LAI/FPAR timeseries; 3) Gap filling the missing values using a spatial-temporal tensor completion model; 4) Generating the SI LAI/FPAR CDR in different projections, spatial and temporal resolutions. The details are described in the following subsections.

3.1 Step1: Filtering the Low-Quality Observations based on QA Values

210   The FparLai_QC and FparExtra_QC layers within the MODIS&VIIRS LAI/FPAR products provide information about the quality of LAI/FPAR, which include algorithm path, cloud and aerosol contaminations, and other factors that lower the reliability of retrievals. Best-quality, high-precision retrievals are obtained from the main algorithm. With a high probability the main algorithm fails in the case of cloud and/or snow-contaminated pixels, or pixels with a high aerosol load (Yan et al., 2021a). As depicted in Table 1, the first step eliminates LAI/FPAR values retrieved by the backup algorithm as well as

215 suspicious values from the main algorithm, which could be affected by clouds, aerosols, and cloud shadows. Note that the quality flags of the Terra-MODIS and Aqua-MODIS products are consistent, while VIIRS slightly differ from the two MODIS QA (e.g., the absence of MODLAND_QC for VIIRS). All three LAI/FPAR products have the same algorithm path and atmospheric conditions. After removing suspicious and low-quality values we get a Filtered Terra/Aqua/VIIRS LAI/FPAR data set.

220 **Table. 1** The quality flags used in the step1.

	Terra	Aqua	VIIRS
MODLAND_QC	Good quality (main algorithm)	Good quality (main algorithm)	×
Retrieval Algorithm Path	main algorithm	main algorithm	main algorithm
Cloud State	Clear or assume clear	Clear or assume clear	Confident clear or probably clear
cloud shadow	No cloud shadow detected	No cloud shadow detected	No cloud shadow
internal cloud mask	No clouds	No clouds	×
Cirrus	No cirrus detected	No cirrus detected	No
LandSea Path	Land	Land	×
Fill value	No	No	No

3.2 Step2: Consolidating the Filtered Terra/Aqua/VIIRS LAI/FPAR into Filtered SI LAI/FPAR Timeseries

       After completing the first step, we obtained three Filtered LAI/FPAR timeseries of different spatial coverage. We consolidated the three timeseries into a Filtered SI LAI/FPAR timeseries as follows. First, a fill value assigned to a pixel, if

there are no high-quality LAI/FPARs from any sensor during the compositing period. Second, if there is only one pair of high-quality LAI and FPAR for the pixel, it is taken as the CDR value with accompanying quality flag set to 1. Finally, if several high-quality retrievals are available for a given pixel during the compositing period, their average is the CDR value. The corresponding quality flag is set to 1 in this case. We generated a 23-year (2000-2022) time series of the Filtered SI LAI/FPAR using this procedure. As (Zhou et al., 2015) argued this timeseries can be used as a reference to estimate an absolute reconstruction error. The reference LAI/FPAR map is shown in Fig. S1 and Fig. S2.

3.3 Step3: Gap Filling the Missing Values Using a Spatial-temporal Tensor Completion Model

Our next step is gap filling, i.e., replacing fill values with estimates of LAI and FPAR. We used a ST-Tensor completion model as our spatial-temporal gap filling method (Chu et al., 2021). This method is particularly well suited for correcting remote sensing images due to its ability to capture intrinsic multidimensional correlations. This technique has proven successful in many applications such as hyperspectral image recovery and reconstruction of missing data in remote sensing images (He et al., 2017;Zheng et al., 2019;Zhang et al., 2019;Chu et al., 2022;Chu et al., 2021). The ST-Tensor completion model used in this study can be broken down into the following four steps.

1) Tensor rearrangement: The LAI/FPAR timeseries have three distinct features. First, they possess spatial neighbourhood similarity based on the first law of geography (Goodchild, 2009). Second, they have temporal neighbourhood correlation, assuming vegetation growth is continuous and smooth (Cong et al., 2012). Finally, they exhibit periodic temporal similarity because vegetation growth varies periodically (Whitt and Ulaby, 1994). While the original tensor form adequately captures spatial neighbourhood similarity and temporal neighbourhood correlation, it does not directly express periodic temporal similarity. Therefore, it is necessary to transform the original tensor into a new tensor that includes all three features. As shown in step 3 of Fig. 2, this study transforms the one-dimensional multi-year time series for each pixel into a two-dimensional matrix. In this matrix, each row represents a one-year time series. At the same time, the two-dimensional spatial image is transformed into a one-dimensional vector. The following equation illustrates this transformation:

$$X_{m*m*T} \rightarrow Y_{m^2*ny*nd} \tag{7}$$

where X is the original tensor, Y is the transformed tensor, m denotes the spatial length of the original tensor, and T denotes the total number of observations in the entire timeseries, which is basically equal to the number of years (ny) multiplied by the number of observations in a year (nd).

2) Iteration updates the weight values and gap fills the missing values: The current third-order tensor can be decomposed into three matrices by three different modes. The tensor rank is defined in different ways and is mainly determined by the correlation and similarity of the elements in the different domains of the tensor. A smaller tensor rank indicates a higher similarity between the values of the tensor elements, which also implies that the missing values are filled consistently across all three dimensions, resulting in the best gap filling. The tensor rank can be defined by considering the three expansion matrices' rank order. Therefore, the data filling process in this study can be represented by the following equation, which aims to optimize problem solving:

$$min \ \sum_{i=1}^{3} w_n \ rank(Y_n) \tag{8}$$

where w_n is the weight corresponding to Y_n that is always non-negative and satisfies $\sum_{i=1}^{3} w_n = 1$. In the process of solving equation (8), it is first necessary to iteratively determine the weight values. We initialize the weights of the three expansion matrices as equal ($w_1 = w_2 = w_3 = 1/3$) and then update them iteratively using the method based on singular value decomposition introduced by (Chu et al., 2021). Once the weight values are obtained, Eq. (8) can be solved efficiently using the algorithm proposed by (Ji et al., 2017). This algorithm uses a logarithmic operator, which better approximates the tensor rank than the classical kernel parameterization, leading to higher accuracy (Ji et al., 2018).

3) Iterate L1 trend filtering: After the ST-Tensor completion process, although a gap-free LAI/FPAR timeseries can be obtained, some residual noise may still exist due to the uncertainties in Flag data. Thus, we employ an iterative L1 trend filtering method, known for its flexibility in denoising one-dimensional timeseries data by regularizing the residual and smoothing terms (Chu et al., 2021;Chu et al., 2022;Eilers, 2003). In this method, we denote the noisy time series as y and the fitted series as z. The objective of the L1 trend filtering method is to balance two conflicting objectives: (a) fidelity to the original series and (b) smoothness of the filtered series. This is achieved by optimizing the following objective function (Eq. 9).

$$Q = \frac{1}{2} \|y - z\|_2^2 + \lambda \|D_z\|_1 \tag{9}$$

where D_z represents the second-order difference matrix and λ is the regularization parameter that balances the fidelity and smoothness terms.

In practice, this method is well suited to preserving the detailed characteristics of turning points, thanks to the L1 parametric constraint. Furthermore, due to the completion of the ST-Tensor process, the remaining noise can be assumed to have a negative bias. In our approach, data with Flag = 0 is considered as noise, while Flag = 1 is considered as almost noiseless. The iterative process is as follows: In the first and second iterations, the L1 trend filter is applied to smooth the LAI/FPAR time series, preserving the good data while replacing only the noisy values that fall below the smoothed series. Subsequent iterations then replace all the noise. By iteratively repeating this process, we achieve a good balance between noise reduction and the preservation of good data. At the end of the filtering step, the results are both gap- and noise-free.

4) Reshape the tensor: Following the reverse process of rearrangement in step 1), the filled and filtered LAI/FPAR tensor is returned to its original form.

3.4 Step4: Generating the SI LAI/FPAR CDR at Different Projections, Spatial and Temporal Resolutions

Our final step aims to generate CDRs at different spatial and temporal resolutions projected on WGS1984 and sinusoidal grids. First, we calculated the bimonthly LAI/FPAR using a weighted averaging method. The spatial resolution of the data was then adjusted to 5 km by nearest neighbour interpolation. Following this step, the projection was transformed from sinusoidal to WGS1984 and the data were further interpolated from a spatial resolution of 500m down to 0.05 degrees using the block average method. As a result of these transformations, we obtained six different versions of the SI LAI/FPAR CDR, as shown

in Table 2. Finally, the SI LAI/FPAR CDR with 500m spatial resolution were uploaded to Google Earth Engine (GEE) for users to mix and match with other datasets and the ease of using this in GEE, all datasets were reprojected to WGS1984 using the gdalwarp function with a crs of EPSG:4326 for ease of ingestion. The other four versions of SI LAI/FPAR CDR can be found in Zenodo (detailed in the section Data Availability).

Table 2. Projections and spatial/temporal resolutions of SI LAI/FPAR CDR.

Resolutions' ID	Projection	Spatial Resolution	Temporal Resolution	Dimensions	Repository
500m_8day	WGS1984	500m	8 days	43200 x 86400 rows/columns	GEE
500m_bimonth	WGS1984	500m	Half month	43200 x 86400 rows/columns	GEE
5km_8day	Sinusoidal	5km	8 days	4320 x 8640 rows/columns	Zenodo
5km_bimonth	Sinusoidal	5km	Half month	4320 x 8640 rows/columns	Zenodo
0.05degree_8day	WGS1984	0.05 degree	8 days	3600 x 7200 rows/columns	Zenodo
0.05degree_bimonth	WGS1984	0.05 degree	Half month	3600 x 7200 rows/columns	Zenodo

4 Results

4.1 Evaluation for the Generating Steps of SI LAI/FPAR CDR over the Amazon Forest

The assessment of vegetation dynamics in the Amazon rainforest, including seasonal changes, is challenging due to persistent cloud cover that interferes with optical remote sensing observations. Therefore, during the evaluation process of the SI LAI/FPAR CDR, each step was assessed using the Amazon Forest region (Fig. 2) as a representative study area. In the first step, considering the significant presence of EBF (50.26%) in the Amazon Forest region, this part compares the LAI/FPAR timeseries from Terra/Aqua/VIIRS before and after filtering the low-quality observations. There is a negative correlation between the RI and the contrast in LAI/FPAR values before and after filtering, which can be explained by significant differences in the quality of retrievals produced by the main and backup algorithms. This filtering process has reduced the magnitude of the LAI variation, leaving their values in the range of 5-6 (Fig. 3), as expected (Samanta et al., 2012a;Samanta et al., 2012b). Filtered FPAR values vary around its inter-annual average of 0.85 (Fig. S3). Furthermore, we observed a consistent intra-annual variation in LAI/FPAR, indicating a clear seasonal dynamic in the EBF.
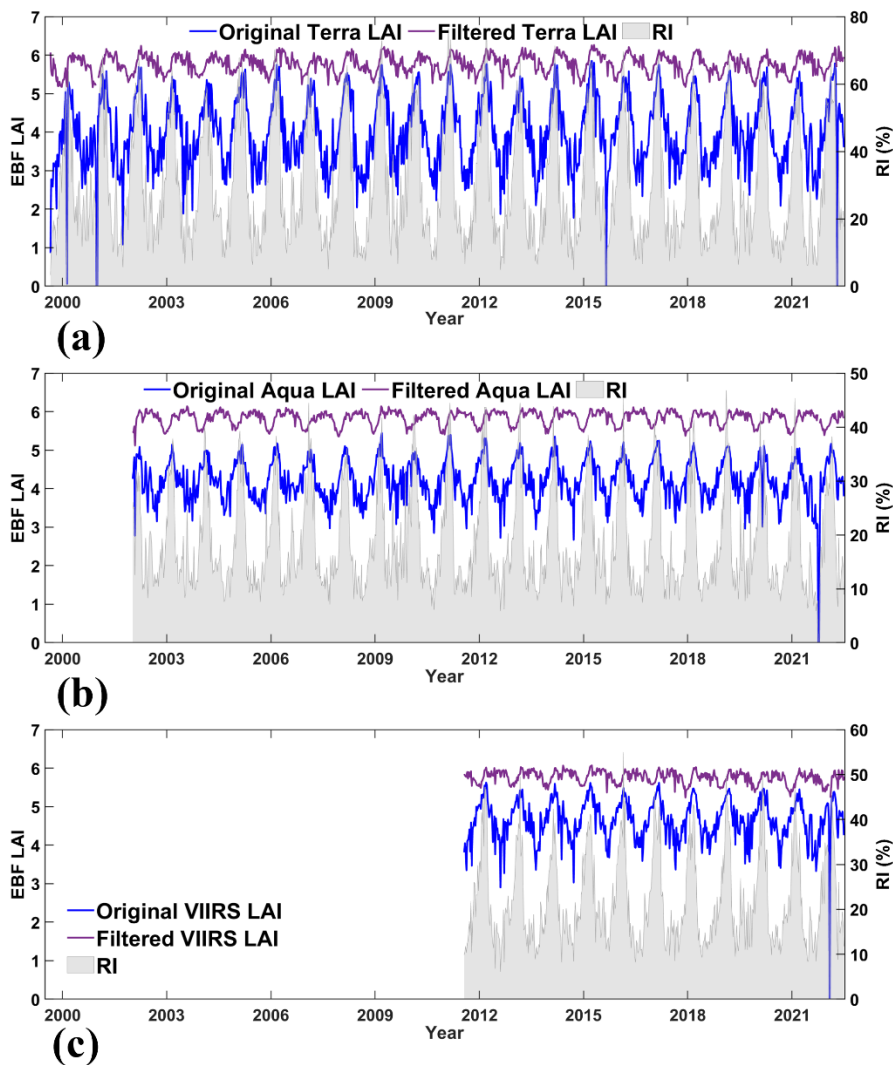
Figure 3. The temporal comparisons between the original Terra/Aqua/VIIRS LAI and Filtered Terra/Aqua/VIIRS LAI for the EBF of Amazon Forest region. The panel (a)~(c) represent Terra/Aqua/VIIRS, respectively. The blue and purple lines mean original and filtered LAI (left y-axis). And the shadow indicates the RI (right y-axis). RI is negatively correlated with the difference between the original and filtered values, suggesting that this procedure reduces the impact of poor-quality retrievals on the time series.

Fig. 4 illustrates percentages of high-quality retrievals from single sensors and after step 2 for selected Amazon Forest region (zoom-in case in Fig. 1) for the 2013 to 2022 overlap period. Table 3 summarizes the changes after the implementation of step 2 for the whole and overlap periods. For the overlap period the percentages increase from 41.09% (Terra), 29.55% (Aqua), and 30.90% (VIIRS) to 58.50% in Filtered SI timeseries. If the time interval is extended to the whole dataset record period (2000 to 2022), the percentages increase from 41.68%, 26.73%, and 14.85% to 54.07%. Consequently, the percentage of pixels that need to be gap filled reaches 45.93%. Table 3 also shows a low frequency of high-quality retrievals available simultaneously from all sensors: 12.45% for the overlap period and 6.02% for the entire acquisition period. Furthermore, Fig.

4 also illustrates that the percentage varies with biome type: it takes values of 46.30% for EBF (northwest region) and 67.51%

320   for savannas (southeast region). Fig. 5 highlights the discontinuity of the spatial-temporal distribution of the quality flag

generated by the data consolidation algorithm (Section. 3.2). For example, the RI for DOY 001 in 2014 (rain season) is 52.66%,

while for DOY 193 in 2014 (dry season) it is 76.63%. This lack of a clear pattern in the spatial-temporal distribution of the

pixels to be gap filled places significant demands on the subsequent filling process.

(a) Filtered Terra RI   **(b) Filtered Aqua RI**

(c) Filtered VIIRS RI   **(d) Filtered Sensor-Independent RI**
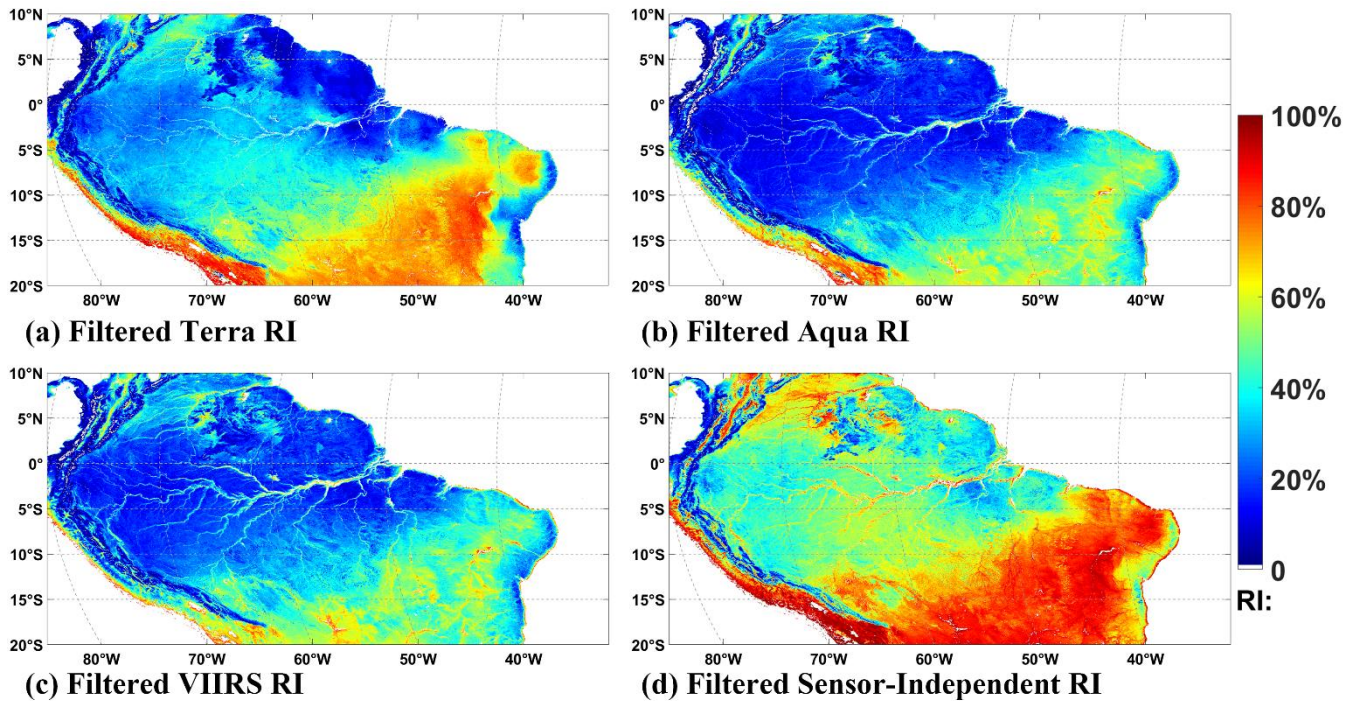
325   **Figure 4.** The spatial distribution of filtered Terra (a), Aqua (b), VIIRS (c), SI (d) RI in the selected Amazon Forest region (zoom-in case in
Fig. 1) in overlap period (2013 to 2022).

Table 3. Percentage of pixels with high-quality retrievals from single sensors and their combinations for whole (2000 to 2022) and overlap
(2013 to 2022) periods. Each row sums to 100%.

2000 ~ 2022	45.93%	20.35%	6.91%	3.62%	11.95%	3.36%	1.85%	6.02%	41.68%	26.73%	14.85%	54.07%

2013 ~ 2022	
No data	41.50%
Terra Only	14.37%
Aqua Only	5.94%
VIIRS Only	7.60%
Terra & Aqua	7.29%
Terra & VIIRS	6.98%
Aqua & VIIRS	3.87%
All Sensors	12.45%
Terra Involved	41.09%
Aqua Involved	29.55%
VIRRS Involved	30.90%
Filtered SI	58.50%

Figure 5. Spatial distribution of the quality flag of the data consolidation algorithm (Sect. 3.2). Panels a and b represent DOYs 1 and 193. Flag value of 0 is grey coded, while other colours correspond to quality flag=1 for various combinations of the sensors. The color

corresponding to Flag=0 represents the No-Sensor category, while the other colors in the figure represent Flag=1. Replace "No Sensor" with "Quality flag=0" and "Non-Veg" with "Non-vegetated land". Delete "Quality Flag" from color bar.
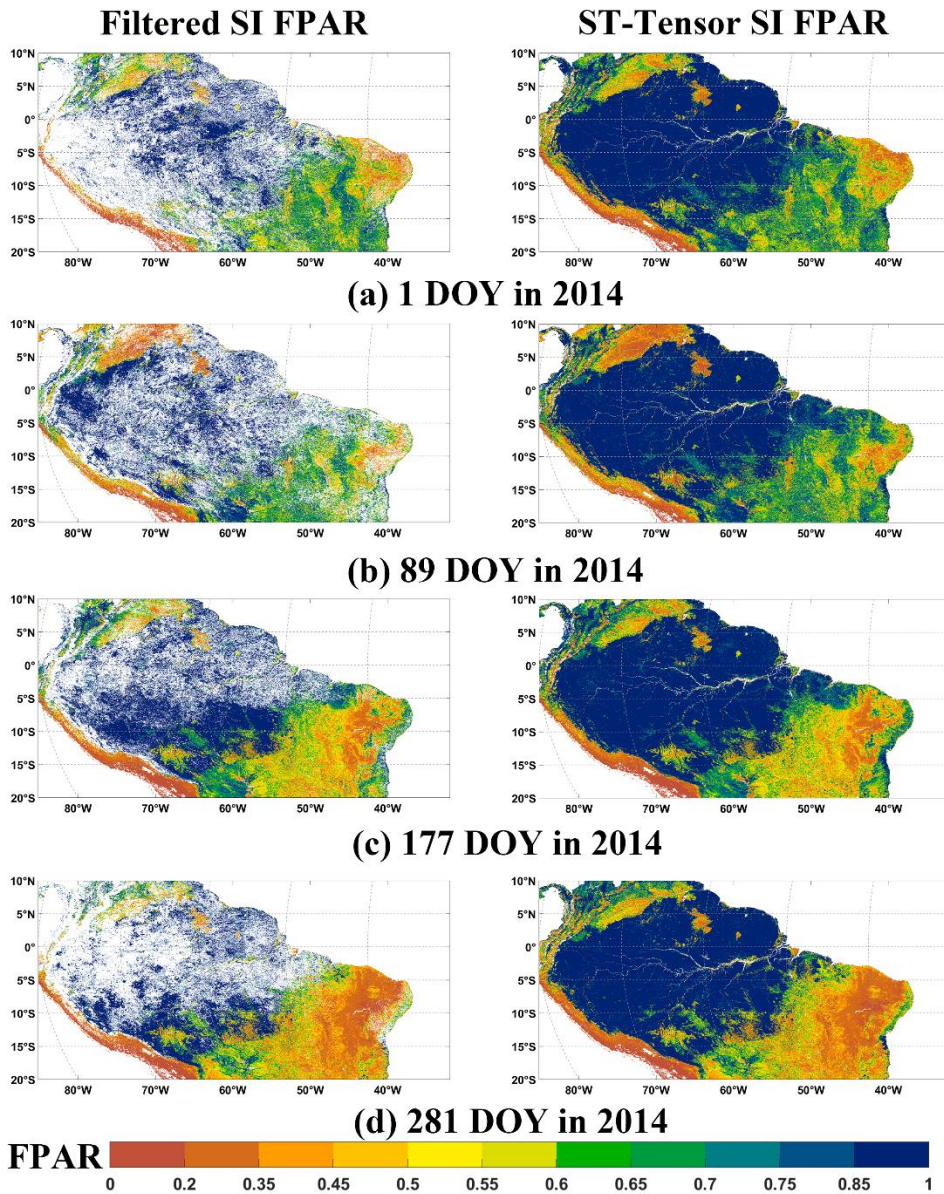
Figure 6. The spatial performance of the ST-Tensor method for DOY 1 (a), 89 (b), 177 (c), 281 (d) in 2014 year in the Amazon Forest region. Left panels and right panels represent the filtered SI LAI and ST-Tensor ST LAI, respectively.

In step3, we replaced fill values with LAI/FPAR estimates produced by the ST-Tensor completion model. The goal of this section is to assess the performance of this technique in terms of whether the recovered pixels are spatial-temporally reasonable. First, Figs 6 and S4 provide compelling visual evidence of the excellent performance achieved by the ST-Tensor completion model. In the spatial domain, it is significant that the LAI/FPAR values obtained after gap filling exhibit a high

concordance with the original high-quality SI LAI/FPAR values of the nearest neighbouring pixels. This underscores the model's ability to preserve spatial consistency. Meanwhile, in the temporal domain, the gap filling LAI/FPAR exhibits highly correlated seasonal variation with biome type at the pixel scale. Furthermore, the improved stability of the LAI/FPAR time series is a notable of this process. In summary, these results collectively emphasize the substantial enhancement in the quality of LAI/FPAR data following the application of the ST-Tensor completion model, both in terms of spatial fidelity and temporal coherence.

4.2 Intercomparison at the Global scale
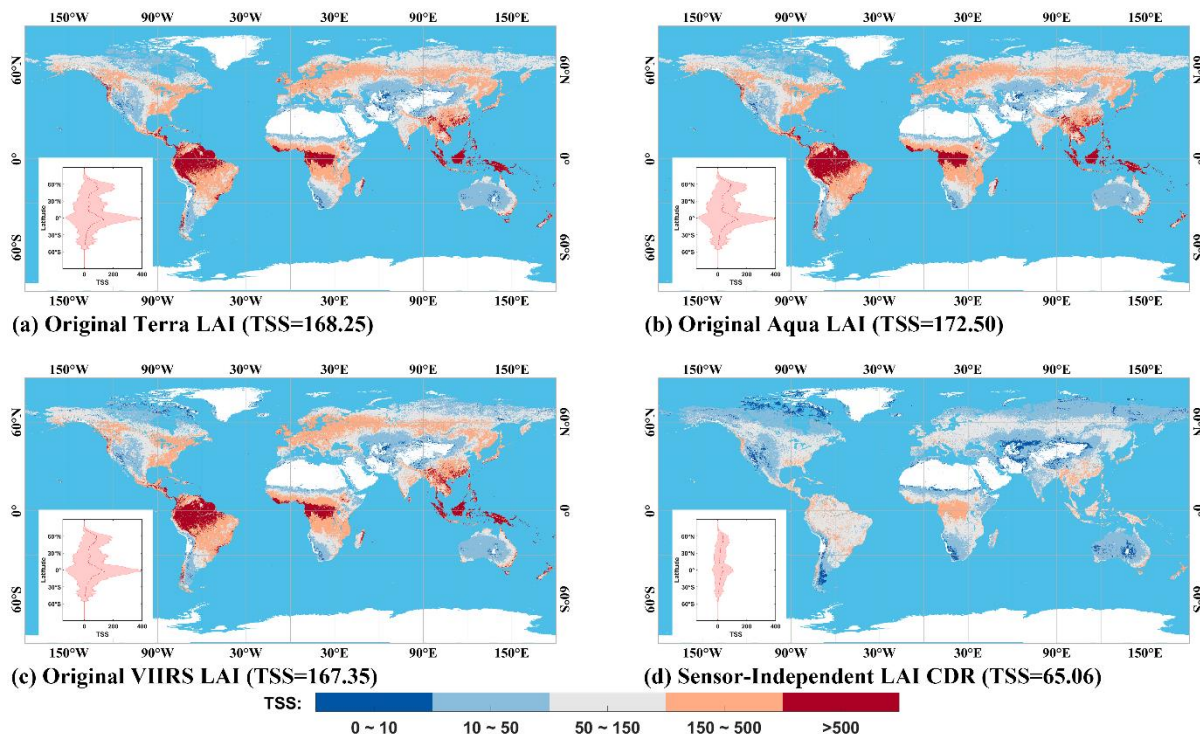
Figure 7. The global distribution of LAI TSS in each 0.05 degree× 0.05 degree grid from 2013 to 2022. Panel (a) –(c) displays the TSS of original Terra/Aqua/VIIRS LAI, respectively. While panel (d) shows the TSS of SI LAI CDR. A WGS1984 projection is used here and the temporal resolution is 8 days. Panels right represent latitudinal transects (0.05 degree interval) of TSS values for LAI. Red lines and shadows represent the mean values and standard deviations of LAI TSS of the 0.05 degree latitude zone.

Here we evaluate the SI LAI/FPAR CDR as well as the LAI/FPAR derived from the original Terra/Aqua/VIIRS data using the TSS and MAE metrics. The results suggest significant improvments in the SI LAI/FPAR CDR compared to the original Terra/Aqua/VIIRS LAI/FPAR data sets. As shown in Figs. 7 – 8 and Figs. S5-S6, SI LAI/FPAR CDR (8-day temporal resolution, 0.05 degree spatial resolution and WGS84 projection) have a higher number of "blue" pixels and lower number of "red" pixels, indicating lower TSS and MAE values. Specifically, the TSS (Fig. 7) of SI LAI CDR (65.06) is much lower than original Terra LAI (168.25), original Aqua LAI (172.50), and original VIIRS LAI (167.35). Similarly, the TSS (Fig. S5) of SI FPAR CDR (12.67) is the lowest compared to the original Terra FPAR (39.68), original Aqua FPAR (41.18), and original

360   VIIRS FPAR (37.94). These indicate that the SI LAI/FPAR CDR has reduced volatility and noise compared to the original versions. The MAE (Fig. 8) shows a similar trend as TSS, with the MAE decreasing from 0.80 (original Terra LAI), 0.79 (original Aqua LAI), and 0.75 (original VIIRS LAI) to 0.39 (SI LAI CDR). And the MAE decreases from 0.16 for the original Terra FPAR, 0.17 for the original Aqua FPAR and 0.16 for original VIIRS FPAR to 0.10 for SI FPAR CDR (Fig. S6). This suggests that the SI LAI/FPAR CDR is more closely related to a high-quality LAI/FPAR reference than the original

365   Terra/Aqua/VIIRS LAI/FPAR. In addition, the variation of TSS/MAE with latitude confirms these improvements, as the SI LAI/FPAR CDR shows smaller mean values and standard deviation of TSS/MAE compared to the original Terra/Aqua/VIIRS LAI/FPAR.

(a) Original Terra LAI (MAE=0.80)   (b) Original Aqua LAI (MAE=0.79)

(c) Original VIIRS LAI (MAE=0.75)   (d) Sensor-Independent LAI CDR (MAE=0.39)
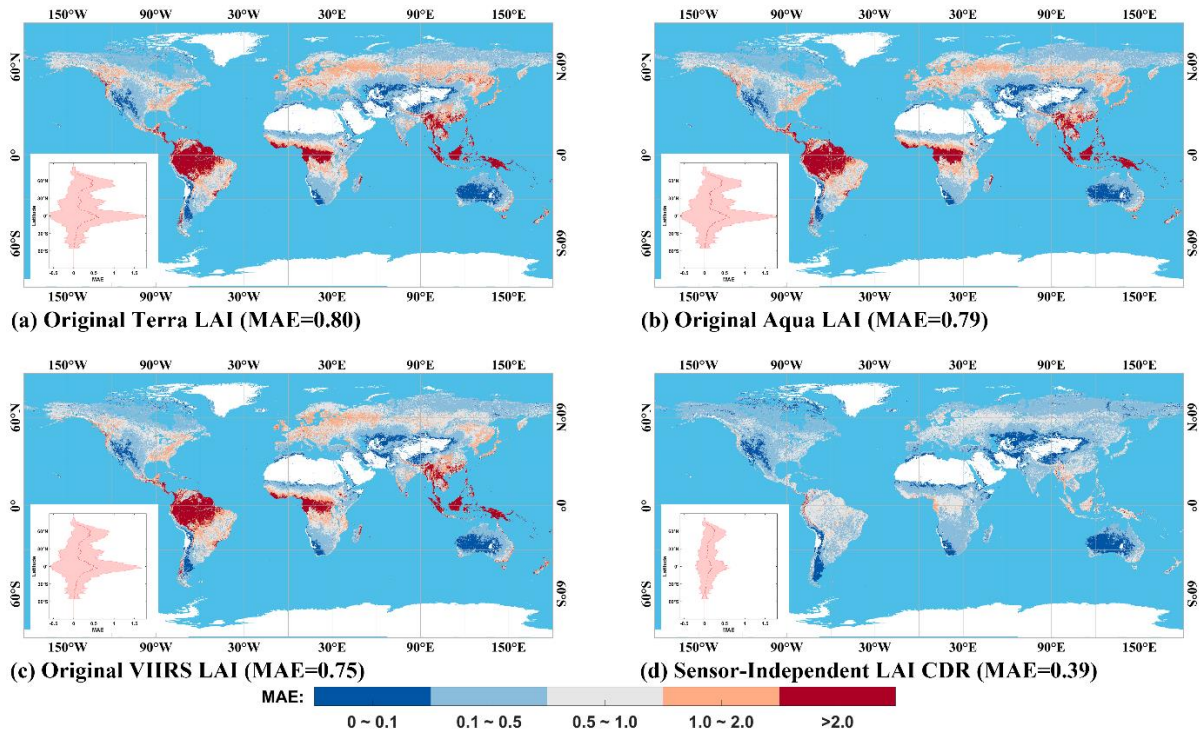
MAE: 0 ~ 0.1   0.1 ~ 0.5   0.5 ~ 1.0   1.0 ~ 2.0   >2.0

Figure 8. Same as Fig. 7 but the metric is MAE. The global distribution of LAI MAE in each 0.05 degree× 0.05 degree grid from 2013 to 370   2022.

    Evidently, these improvements are particularly noticeable in the selected Amazon Forest region, where both the TSS and MAE of SI LAI/FPAR CDR show significant decreasing trend compared to the original Terra/Aqua/VIIRS LAI/FPAR (Figs. S7 – S10). The magnitude decrease of TSS for SI LAI/FPAR CDR is above 300/60, and the magnitude decrease of MAE is above 1.5/0.2, which exceeds other global regions. This implies a significant improvement in the SI LAI/FPAR CDR,

375   especially when dealing with large amounts of missing data. Furthermore, similar improvements are observed when the temporal resolution is bimonthly (Figs. S11 – S14). Overall, these results highlight the significant improvement achieved with the SI LAI/FPAR CDR over the original Terra/Aqua/VIIRS LAI/FPAR, demonstrating its enhanced performance and accuracy.

4.3 Validation Using Ground LAI/FPAR Measurements
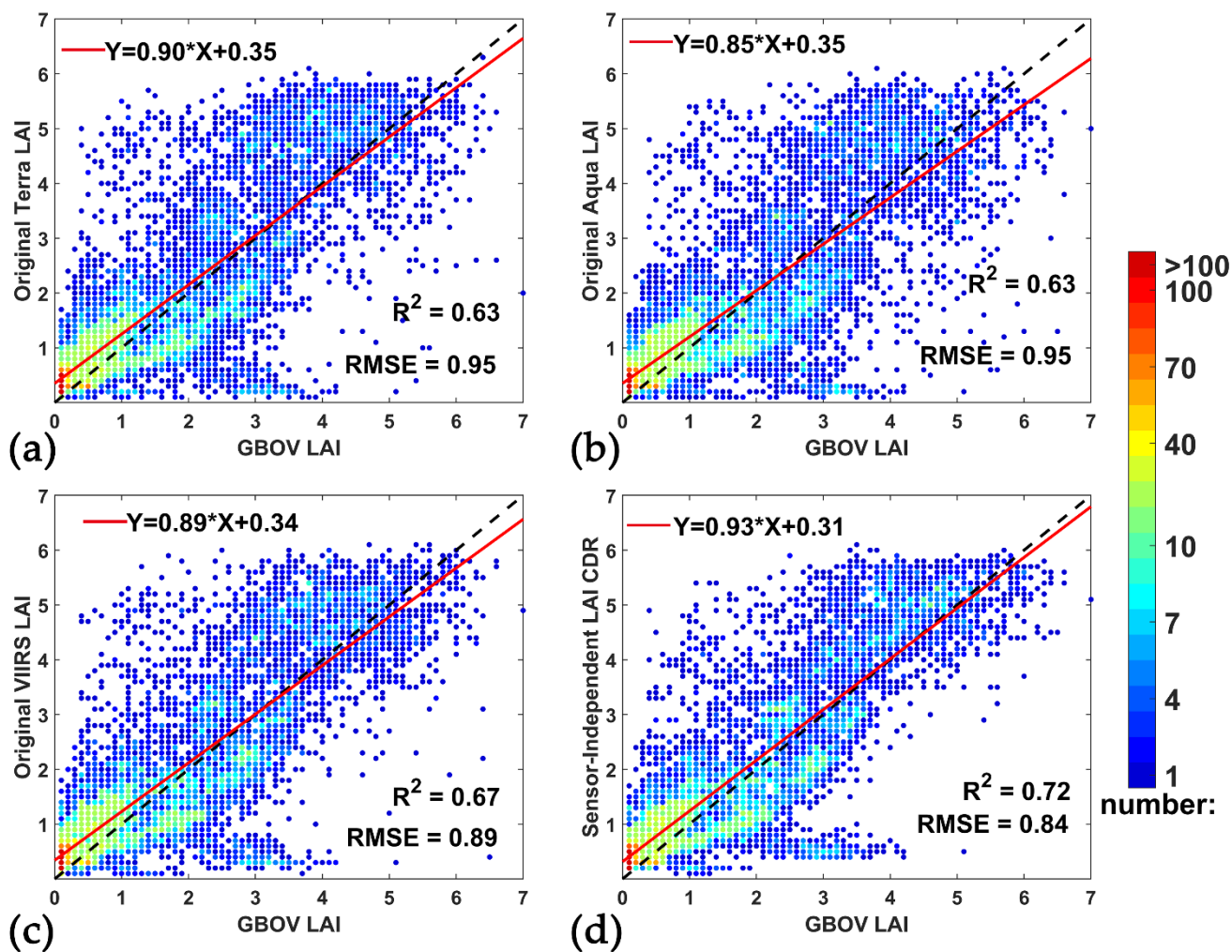
Figure 9. Comparisons of original Terra/Aqua/VIIRS LAI and SI LAI CDR with ground GBOV LAI. The bin for X and Y axis is 0.1 and the color means the number of pixels in this bin.

380
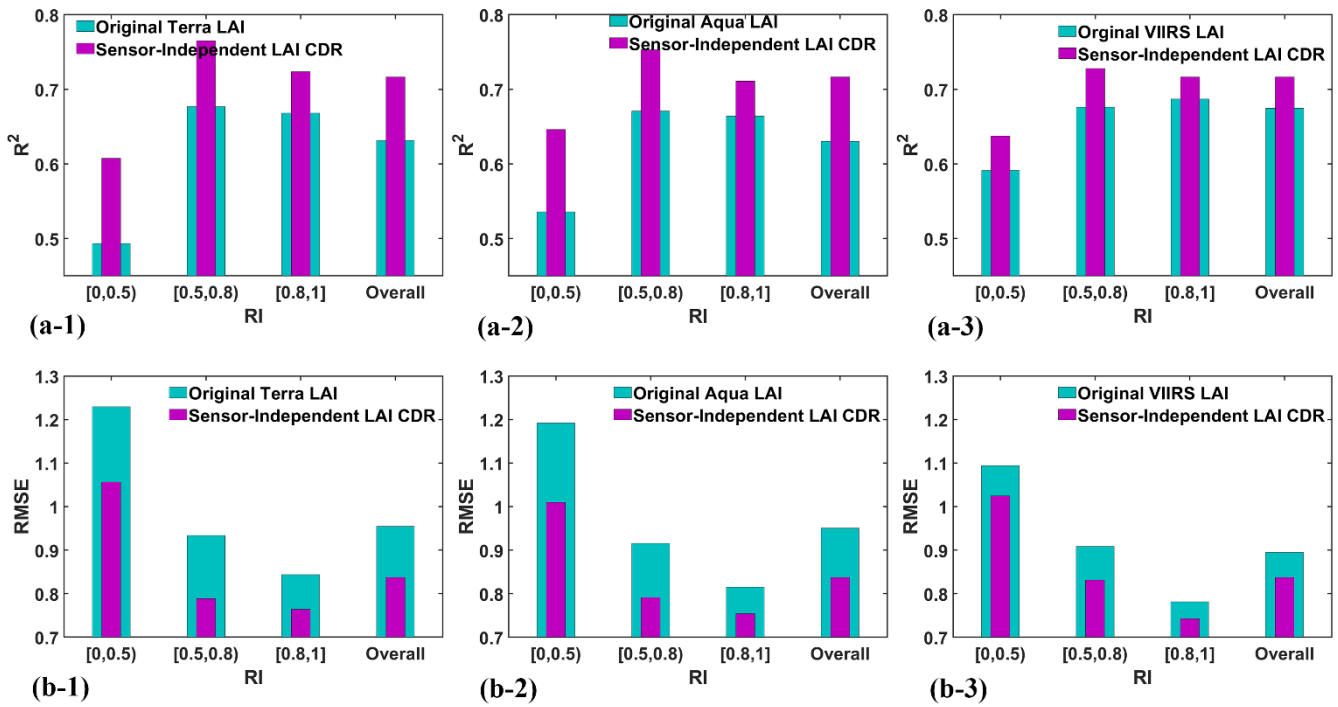
Figure 10. The R^2 and RMSE between original Terra/Aqua/VIIRS LAI and SI LAI CDR and GBOV LAI in different RI ranges.

385   Fig 9 shows comparisons of the SI LAI CDR and original Terra/Aqua/VIIRS LAI with the GBOV ground data. The SI LAI CDR shows highest accuracy, as evidenced by R^2 = 0.72 and RMSE = 0.84. Followed by the original VIIRS LAI (R^2 = 0.67 and RMSE = 0.89) and then the original Terra/Aqua LAI (R^2 = 0.63 and RMSE = 0.95 for both Terra/Aqua). Similar results are observed in the case of FPAR, where the SI FPAR CDR outperforms the original Terra/Aqua/VIIRS FPAR. The R^2 values increased from original Terra/Aqua/VIIRS FPAR by 0.74/0.72/0.76 to 0.79 (SI FPAR CDR), while the RMSE

390   decrease from 0.17/0.18/0.16 to 0.15 (Fig. S15). It is important to note that all datasets show a tendency to overestimate low LAI/FPAR values and underestimate high FPAR values. However, the SI LAI/FPAR CDR shows a closer fit to the 1:1 line compared to the original Terra/Aqua/VIIRS LAI/FPAR. In addition, the SI LAI/FPAR CDR shows significant improvements across all RI ranges. The R^2 values increased by approximately 0.02 to 0.21 from the original Terra/Aqua/VIIRS LAI/FPAR to SI LAI/FPAR CDR, while the RMSE values decrease by approximately 0.01 to 0.22 (Fig. 10 and Fig. S16). Especially the

395   RI in the range of [0, 0.5), the enhancements were the most significant among all RI ranges for both Terra/Aqua/VIIRS, which indicates that the SI LAI/FPAR CDR represents a significant improvement over the LAI/FPAR obtained using the backup algorithm.
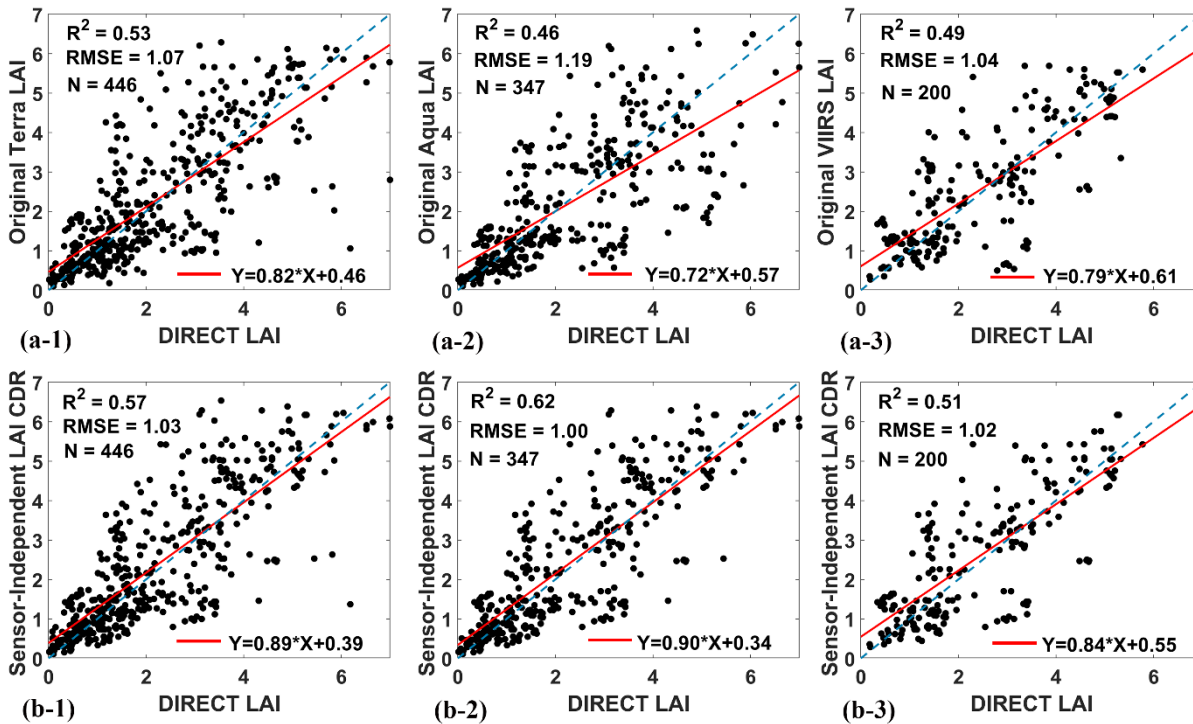
Figure 11. Comparisons of original Terra/Aqua/VIIRS LAI and SI LAI CDR with ground DIRECT2.1 LAI measurements. The numbers corresponding to N in the top plot are the number of all DIRECT measurements for the period covered by Terra/Aqua/VIIRS, respectively, and the N in the bottle plot corresponds to N in the top plots, respectively.

Improvements were also observed based on comparisons with the DIRECT ground truth data. Compared to the original Terra/Aqua/VIIRS LAI, the R^2 values of SI LAI CDR increased by 0.04/0.14/0.02, while the RMSE values showed a decrease by 0.04/0.19/0.02 (Fig. 11). Similarly, there is an increasing trend in R^2 of 0.09/0.05/0.06 for FPAR, accompanied by a decreasing trend in RMSE of 0.02/0.01/0.02 (Fig. S17). The improvement from original Aqua LAI to SI LAI CDR was the most pronounced in LAI, with R^2 increasing from 0.46 to 0.62 and RMSE decreasing from 1.19 to 1.00. The improvement from original Terra FPAR to SI FPAR CDR was the most pronounced in FPAR, with R^2 increasing from 0.71 to 0.82 and RMSE decreasing from 0.13 to 0.11. The improvement is also reflected in the fact that the SI LAI/FPAR CDR scatters vs. DIRECT LAI/FPAR are closer to the 1:1 line.
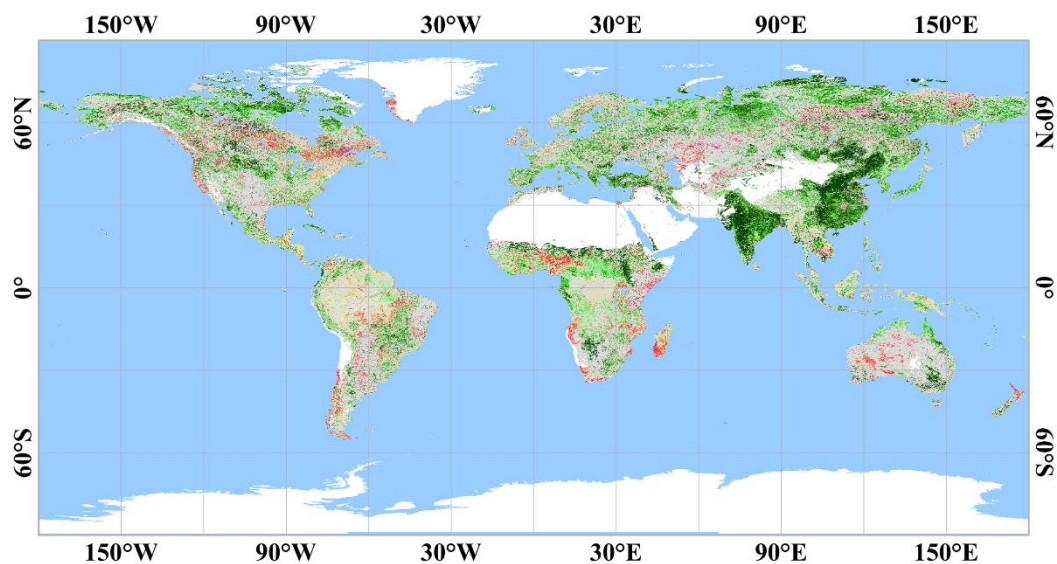
(a) Sensor-Independent LAI CDR
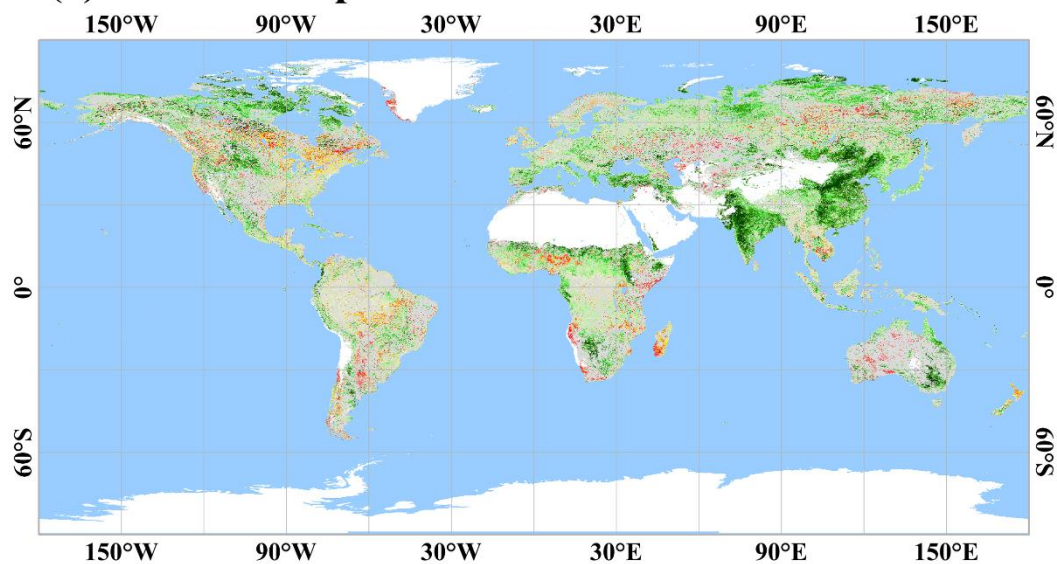
(b) Sensor-Independent FPAR CDR
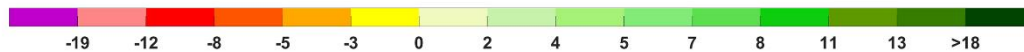
Trend in annual average LAI/FPAR from 2001 to 2022 (%/decade)

Figure 12. Map of trends in annual average SI LAI/FPAR for 2001–2022. Statistically significant trends (Mann–Kendall test, P≤ 0.05) are color-coded. Grey areas show vegetated land with statistically insignificant trends. White areas depict barren lands, permanent ice-covered areas, permanent wetlands, and built-up areas. Blue areas represent water.

415   Previous studies have shown a significant greening trend in global leaf area (Zhang et al., 2017;Chen et al., 2019;Cortés et al., 2021). However, loss of sensor calibration, atmospheric contamination of the vegetation signal influenced the previous studies. Thus, this study aims to provide further insight into 'Greening Earth' by analysing the high-quality SI LAI/FPAR CDR. The results obtained from this study provide a clear indication of the greening trend of vegetation. Specifically, according to SI LAI CDR, almost one-third (30.71%) of the vegetated areas are greening and only 6.67% of the vegetated areas show a

420   browning trend (Fig. 12a). These findings are also supported by the results of the SI FPAR CDR, where about 31.26% of the vegetated area is greening and only 6.50% is browning (Fig. 12b). In terms of overall global vegetation status, the analysis suggests a significant increase in greenness from 2001 to 2022. The LAI shows a significant increasing trend of 2.33% per decade and the FPAR also shows a significant increasing trend of 1.93% per decade, which can be translated to a constant net increase in leaf area. Focus on individual regions, SI LAI/FPAR CDR also highlights the significant contribution of China and

425   India to the global greening trend. These regions show significant increases in vegetation greenness, supporting the overall global trend observed in the analysis. While there are scattered browning trend in the high latitudes of the northern hemisphere, south Africa, and Amazon Forest region.

5 Discussion

Improving the quality of LAI/FPAR timeseries is crucial to ensure the reliability of vegetation studies. Therefore, it is

430   necessary to explore various techniques of post-processing satellite-derived LAI/FPAR. In the operational data processing, the main RT-based algorithm produces best quality and high precision parameters. With a high probability the main algorithm fails in the case of cloud and/or snow contaminated pixels, or pixels with a high aerosol load. When this happens, the backup method is utilized. This causes high frequency noise in the LAI/FPAR time series, which indirectly leads to time series instability and absolute accuracy problems. Therefore, the first step in the developing SI LAI/FPAR CDR production process

435   was to eliminate poor quality retrievals to ensure that subsequent steps such as gap filling are not affected by noise. As a result, the first step filtering principle is also relatively more stringent. Previous studies on the reconstruction of MODIS&VIIRS LAI time series often only filter the backup algorithm (Huang et al., 2021) but this study also filters the main algorithm that have been affected by clouds and aerosols. The findings after step 1 are consistent with previous studies investigating the dynamics of vegetation phenology in tropical rainforest (Myneni et al., 2007;Samanta et al., 2012a;Hashimoto et al., 2021;Sun et al.,

440   2022), which also indirectly proves the necessity of this step.

The current MODIS&VIIRS LAI/FPAR retrieval algorithm considers the effect of SZA on LAI, but also FPAR depends on SZA (Knyazikhin et al., 1998a;Pu et al., 2020). The newly proposed SI LAI/FPAR CDR differs from the previously reconstructed sensor-dependent time series by its SI feature, which includes both morning and afternoon high-quality retrievals. By accounting for the effects of satellite transit times at different times of the day, particularly in relation to SZA

445   variations, the SI LAI/FPAR CDR avoids potential systematic biases. Thus, the SI property allows FPAR to be unaffected by

a single observation. In addition, the process of consolidating the original Terra/Aqua/VIIRS LAI/FPAR into a SI LAI/FPAR CDR also provides as much information as possible for the subsequent gap filling step (Ganguly et al., 2008;Xiao et al., 2014).

In recent years, numerous spatial-temporal reconstruction methods have been proposed from different perspectives. However, most of these methods are based on empirical filtering and function fitting approaches, neglecting the use of prior information or statistical properties. The ST-Tensor model used in this study differs from previous models in that it considers the strong correlation between temporal and spatial scales (Chu et al., 2021). In addition, the ST-Tensor model considers the consistency of variability across years, effectively exploiting the internal correlation of the LAI/FPAR (Ji et al., 2018;Li et al., 2019). As a result, the gap filled LAI/FPAR shows a high degree of consistency with the original high-quality data, thus preserving the integrity of the original measurements. This reduction in the frequency of noise within the LAI/FPAR time series is highly beneficial for phenology studies and agricultural management. Additionally, the L1 trend iteration step of the ST-Tensor model ensures that certain anomalous observations, such as forest degradation due to fire, are not inadvertently smoothed by the algorithm. This capability contributes to the reliability and accuracy of the model.

This study establishes the accuracy of the SI LAI/FPAR CDR through direct ground validation, which includes rigorous evaluation against ground measurements and related metrics. The results of this validation process demonstrate the reliability of the product. Furthermore, we also compared the above analysing results (section 4.4) reported by a recent study (Chen et al., 2019;Zhang et al., 2017), both greening and browning trends are consistent. These results confirm the previous understanding of 'Greening Earth' and indirectly prove the reliability of SI LAI/FPAR CDR. The SI LAI/FPAR CDR analysis provides a valuable tool for monitoring and understanding the dynamics of global vegetation change. The consistency of the study's results with those of previous research adds to the robustness and credibility of the product. The provision of multiple spatial and temporal resolution versions of the SI LAI/FPAR CDR in this study greatly enhances the ability to study global and local vegetation change and climate dynamics.

6 Conclusions

This study developed a SI LAI/FPAR CDR based on Terra-MODIS/Aqua-MODIS/VIIRS LAI/FPAR standard products and ST-Tensor completion model. The CDR covers a substantial temporal period from 2000 to 2022, with spatial resolutions of 500m/5km/0.05 degrees and temporal resolutions of 8 days or half month. The generation of the SI LAI/FPAR CDR was evaluated at each step, including the evaluation of every step and ST-Tensor completion model. Evaluation results show that the elimination of low-quality LAI/FPAR and consolidating Terra/Aqua/VIIRS LAI/FPAR into SI LAI/FPAR are effective in the production process; and the ST-Tensor completion model was excelled in gap filling. The ground-based validations show that the newly generated SI LAI/FPAR CDR achieves higher accuracy compared to original Terra/Aqua/VIIRS LAI/FPAR products. Specifically, the SI LAI/FPAR CDR shows the highest accuracy (R^2 = 0.72/0.79 and RMSE = 0.84/0.15 for LAI/FPAR) among all LAI/FPAR products with GBOV LAI/FPAR as benchmark. Similarly, the SI LAI/FPAR CDR shows an increase R^2 magnitude of 0.04~0.16/0.05~0.09 and a decrease RMSE magnitude of 0.02~0.19/0.01~0.02 based on DIRECT

LAI/FPAR. The evaluation results also shows that the SI LAI/FPAR CDR has a lower TSS compared to the original Terra/Aqua/VIIRS LAI/FPAR product, which suggests that this CDR has less noise and provides more stable timeseries.

480 Conversely, the MAE is also lower, indicating that the SI LAI/FPAR CDR is closer to high-quality LAI/FPAR retrievals compared to Terra/Aqua/VIIRS LAI/FPAR products. Additionally, the reproduce results of the 'Greening Earth' study demonstrate the consistency of trend analysis based on the SI LAI/FPAR CDR with previous findings. The same consistency analysis greatly enhances the ability to conduct further studies on vegetation dynamics and climate change. By exploiting the integration of multiple satellite data sources and applying advanced gap-filling techniques, the SI LAI/FPAR CDR presented

485 in this study provides a valuable resource for researchers studying vegetation dynamics and their relationship to climate change. Overall, the rigorous evaluation and validation conducted throughout the study provides confidence in the accuracy and reliability of the SI LAI/FPAR CDR, further strengthening its utility for diverse applications in environmental science and land management.

Data availability.

490   The SI LAI/FPAR CDR is openly available at: https://doi.org/10.5281/zenodo.8076540 (Pu et al., 2023a), https://code.earthengine.google.com/?asset=projects/sat-io/open-datasets/BU_LAI_FPAR/wgs_500m_8d, https://code.earthengine.google.com/?asset=projects/sat-io/open-datasets/BU_LAI_FPAR/wgs_500m_bimonthly.

And the Readme files about data description, data availability, and example code of GEE and MATLAB for SI LAI/FPAR CDR can be found at https://github.com/JiabinPu/Sensor-Independent-LAI-FPAR-CDR.

495 **CRediT Author Statement.**

JP: Methodology, Conceptualization, Software, Formal analysis, Writing - Original Draft. **KY:** Methodology, Conceptualization, Draft Revision, Supervision. **SR:** Dataset Management, Resources. **ZZ:** Draft Review and Revision. **MR:** Draft Review and Revision. **YK:** Formal analysis, Draft Revision, Supervision, Resources. **RM:** Conceptualization, Resources, Supervision.

500 **Competing Interests.**

The authors declare that they have no known competing financial interests or personal relationships that could have influenced the work reported in this study.

Disclaimer.

Publisher's note: Copernicus Publications remains neutral with regard to jurisdictional claims in published maps and institutional affiliations.

Acknowledgments.

We would like to thank NASA for providing MODIS&VIIRS standard products. We gratefully acknowledge the Google Earth Engine (https://earthengine.google.com/). We also like to thank Dong Chu in Wuhan University for the code of ST-Tensor completion model code.

Financial Support.

This work was supported by the NASA Grants to Boston University under the MODIS and VIIRS Projects (80NSSC21K1925 and 80NSSC21K1960).

References

1. Bai, G., Lerebourg, C., Brown, L., Morris, H., Dash, J., Clerici, M., and Gobron, N.: GBOV (Ground-Based Observation for Validation): A Copernicus Service for Validation of Land Products, 2022.
2. Baret, F., Morissette, J. T., Fernandes, R. A., Champeaux, J. L., Myneni, R. B., Chen, J., Plummer, S., Weiss, M., Bacour, C., and Garrigues, S.: Evaluation of the representativeness of networks of sites for the global validation and intercomparison of land biophysical products: Proposition of the CEOS-BELMANIP, IEEE Transactions on Geoscience Remote Sensing, 44, 1794-1803, https://doi.org/10.1109/TGRS.2006.876030, 2006.
3. Boussetta, S., Balsamo, G., Beljaars, A., Kral, T., and Jarlan, L.: Impact of a satellite-derived leaf area index monthly climatology in a global numerical weather prediction model, International journal of remote sensing, 34, 3520-3542, https://doi.org/10.1080/01431161.2012.716543, 2013.
4. Brown, L. A., Meier, C., Morris, H., Pastor-Guzman, J., Bai, G., Lerebourg, C., Gobron, N., Lanconelli, C., Clerici, M., and Dash, J.: Evaluation of global leaf area index and fraction of absorbed photosynthetically active radiation products over North America using Copernicus Ground Based Observations for Validation data, Remote Sensing of Environment, 247, 111935, https://doi.org/10.1016/j.rse.2020.111935, 2020.
5. Brown, L. A., Camacho, F., García-Santos, V., Origo, N., Fuster, B., Morris, H., Pastor-Guzman, J., Sánchez-Zapero, J., Morrone, R., and Ryder, J.: Fiducial reference measurements for vegetation bio-geophysical variables: an end-to-end uncertainty evaluation framework, Remote Sensing, 13, 3194, https://doi.org/10.3390/rs13163194, 2021.
6. Chen, C., Park, T., Wang, X., Piao, S., Xu, B., Chaturvedi, R. K., Fuchs, R., Brovkin, V., Ciais, P., Fensholt, R., Tommervik, H., Bala, G., Zhu, Z., Nemani, R. R., and Myneni, R. B.: China and India lead in greening of the world through land-use management, Nat Sustain, 2, 122-129, https://doi.org/10.1038/s41893-019-0220-7, 2019.
7. Chen, C., Riley, W. J., Prentice, I. C., and Keenan, T. F.: CO2 fertilization of terrestrial photosynthesis inferred from site to global scales, Proceedings of the National Academy of Sciences, 119, e2115627119, https://doi.org/10.1073/pnas.2115627119, 2022.
8. Chen, J. M., and Black, T. A.: Defining leaf area index for non-flat leaves, Plant, Cell & Environment, 15, 421-429, https://doi.org/10.1111/j.1365-3040.1992.tb00992.x, 1992.
9. Chen, J. M.: Optically-based methods for measuring seasonal variation of leaf area index in boreal conifer stands, Agricultural and Forest Meteorology, 80, 135-163, https://doi.org/10.1016/0168-1923(95)02291-0, 1996.
10. Chu, D., Shen, H., Guan, X., Chen, J. M., Li, X., Li, J., and Zhang, L.: Long time-series NDVI reconstruction in cloud-prone regions via spatio-temporal tensor completion, Remote Sensing of Environment, 264, 112632, https://doi.org/10.1016/j.rse.2021.112632, 2021.

11. Chu, D., Shen, H., Guan, X., and Li, X.: An L1-regularized variational approach for NDVI time-series reconstruction considering inter-annual seasonal similarity, International Journal of Applied Earth Observation and Geoinformation, 114, 103021, https://doi.org/10.1016/j.jag.2022.103021, 2022.

12. Cong, N., Piao, S., Chen, A., Wang, X., Lin, X., Chen, S., Han, S., Zhou, G., and Zhang, X.: Spring vegetation green-up date in China inferred from SPOT NDVI data: A multiple model analysis, Agricultural and Forest Meteorology, 165, 104-113, https://doi.org/10.1016/j.agrformet.2012.06.009, 2012.

13. Cortés, J., Mahecha, M. D., Reichstein, M., Myneni, R. B., Chen, C., and Brenning, A.: Where are global vegetation greening and browning trends significant?, Geophysical Research Letters, 48, e2020GL091496, https://doi.org/10.1029/2020GL091496, 2021.

14. Das, M., and Ghosh, S. K.: A deep-learning-based forecasting ensemble to predict missing data for remote sensing analysis, IEEE Journal of Selected Topics in Applied Earth Observations and Remote Sensing, 10, 5228-5236, https://doi.org/10.1109/JSTARS.2017.2760202, 2017.

15. Dong, Y., Li, J., Jiao, Z., Liu, Q., Zhao, J., Xu, B., Zhang, H., Zhang, Z., Liu, C., and Knyazikhin, Y.: A method for retrieving coarse-resolution leaf area index for mixed biomes using a mixed-pixel correction factor, IEEE Transactions on Geoscience and Remote Sensing, https://doi.org/10.1109/TGRS.2023.3235949, 2023.

16. Eilers, P. H.: A perfect smoother, Analytical chemistry, 75, 3631-3636, https://doi.org/10.1021/ac034173t, 2003.

17. Fang, H., Wei, S., Jiang, C., and Scipal, K.: Theoretical uncertainty analysis of global MODIS, CYCLOPES, and GLOBCARBON LAI products using a triple collocation method, Remote Sensing of Environment, 124, 610-621, https://doi.org/10.1016/j.rse.2012.06.013, 2012a.

18. Fang, H., Wei, S., and Liang, S.: Validation of MODIS and CYCLOPES LAI products using global field measurement data, Remote Sensing of Environment, 119, 43-54, https://doi.org/10.1016/j.rse.2011.12.006, 2012b.

19. Fang, H., Baret, F., Plummer, S., and Schaepman-Strub, G.: An overview of global leaf area index (LAI): Methods, products, validation, and applications, Reviews of Geophysics, 57, 739-799, https://doi.org/10.1029/2018RG000608, 2019.

20. Ganguly, S., Schull, M. A., Samanta, A., Shabanov, N. V., Milesi, C., Nemani, R. R., Knyazikhin, Y., and Myneni, R. B.: Generating vegetation leaf area index earth system data record from multiple sensors. Part 1: Theory, Remote Sensing of Environment, 112, 4333-4343, https://doi.org/10.1016/j.rse.2008.07.014, 2008.

21. Goodchild, M. F.: First law of geography, in: International encyclopedia of human geography, Elsevier Inc., 179-182, 2009.

22. Hamed, K. H., and Rao, A. R.: A modified Mann-Kendall trend test for autocorrelated data, Journal of hydrology, 204, 182-196, https://doi.org/10.1016/S0022-1694(97)00125-X, 1998.

23. Hashimoto, H., Wang, W., Dungan, J. L., Li, S., Michaelis, A. R., Takenaka, H., Higuchi, A., Myneni, R. B., and Nemani, R. R.: New generation geostationary satellite observations support seasonality in greenness of the Amazon evergreen forests, Nature Communications, 12, 684, https://doi.org/10.1038/s41467-021-20994-y, 2021.

24. He, W., Zhang, H., and Zhang, L.: Total variation regularized reweighted sparse nonnegative matrix factorization for hyperspectral unmixing, IEEE Transactions on Geoscience and Remote Sensing, 55, 3909-3921, https://doi.org/10.1109/TGRS.2017.2683719, 2017.

25. Holben, B. N.: Characteristics of maximum-value composite images from temporal AVHRR data, International journal of remote sensing, 7, 1417-1434, https://doi.org/10.1080/01431168608948945, 1986.

26. Huang, A., Shen, R., Di, W., and Han, H.: A methodology to reconstruct LAI time series data based on generative adversarial network and improved Savitzky-Golay filter, International Journal of Applied Earth Observation and Geoinformation, 105, 102633, https://doi.org/10.1016/j.jag.2021.102633, 2021.

27. Ji, T.-Y., Huang, T.-Z., Zhao, X.-L., Ma, T.-H., and Deng, L.-J.: A non-convex tensor rank approximation for tensor completion, Applied Mathematical Modelling, 48, 410-422, https://doi.org/10.1016/j.apm.2017.04.002, 2017.

28. Ji, T.-Y., Yokoya, N., Zhu, X. X., and Huang, T.-Z.: Nonlocal tensor completion for multitemporal remotely sensed images' inpainting, IEEE Transactions on Geoscience and Remote Sensing, 56, 3047-3061, https://doi.org/10.1109/TGRS.2018.2790262, 2018.

29. Justice, C. O., Román, M. O., Csiszar, I., Vermote, E. F., Wolfe, R. E., Hook, S. J., Friedl, M., Wang, Z., Schaaf, C. B., and Miura, T.: Land and cryosphere products from Suomi NPP VIIRS: Overview and status, Journal of Geophysical Research: Atmospheres, 118, 9753-9765, https://doi.org/10.1002/jgrd.50771, 2013.

30. Knyazikhin, Y., Martonchik, J., Myneni, R. B., Diner, D., and Running, S. W.: Synergistic algorithm for estimating vegetation canopy leaf area index and fraction of absorbed photosynthetically active radiation from MODIS and MISR data, Journal of Geophysical Research: Atmospheres, 103, 32257-32275, https://doi.org/10.1029/98JD02462, 1998a.

31. Knyazikhin, Y., Martonchik, J. V., Diner, D. J., Myneni, R. B., Verstraete, M. M., Pinty, B., and Gobron, N.: Estimation of vegetation canopy leaf area index and fraction of absorbed photosynthetically active radiation from atmosphere-corrected MISR data, Journal of Geophysical Research, 103, 32239-32256, https://doi.org/10.1029/98JD02461, 1998b.

32. Knyazikhin, Y.: MODIS leaf area index (LAI) and fraction of photosynthetically active radiation absorbed by vegetation (FPAR) product (MOD 15) algorithm theoretical basis document, https://modis.gsfc.nasa.gov/data/atbd/atbd_mod15.pdf, 1999.

33. Knyazikhin, Y., and Myneni, R.: VIIRS leaf area index (LAI) and fraction of photosynthetically active radiation absorbed by vegetation (FPAR) user guide, https://lpdaac.usgs.gov/documents/126/VNP15_User_Guide.pdf, 2018.

34. Lange, M., Dechant, B., Rebmann, C., Vohland, M., Cuntz, M., and Doktor, D.: Validating MODIS and sentinel-2 NDVI products at a temperate deciduous forest site using two independent ground-based sensors, Sensors, 17, 1855, https://doi.org/10.3390/s17081855, 2017.

35. Li, X.-T., Zhao, X.-L., Jiang, T.-X., Zheng, Y.-B., Ji, T.-Y., and Huang, T.-Z.: Low-rank tensor completion via combined non-local self-similarity and low-rank regularization, Neurocomputing, 367, 1-12, 2019.

36. Mariano, D. A., Santos, C. A. C. D., Wardlow, B. D., Anderson, M. C., Schiltmeyer, A. V., Tadesse, T., and Svoboda, M.: Use of remote sensing indicators to assess effects of drought and human-induced land degradation on ecosystem health in Northeastern Brazil, Remote Sensing of Environment, 213, 129-143, https://doi.org/10.1016/j.rse.2018.04.048, 2018.

37. Merchant, C. J., Paul, F., Popp, T., Ablain, M., Bontemps, S., Defourny, P., Hollmann, R., Lavergne, T., Laeng, A., and De Leeuw, G.: Uncertainty information in climate data records from Earth observation, Earth System Science Data, 9, 511-527, https://doi.org/10.5194/essd-9-511-2017, 2017.

38. Mitášová, H., and Hofierka, J.: Interpolation by regularized spline with tension: II. Application to terrain modeling and surface geometry analysis, Mathematical geology, 25, 657-669, https://doi.org/10.1007/BF00893172, 1993.

39. Myneni, R., Knyazikhin, Y., and Park, T.: MOD15A2H MODIS/Terra Leaf Area Index/FPAR 8-Day L4 Global 500m SIN Grid V006. NASA EOSDIS Land Processes Distributed Active Archive Center, 2015.

40. Myneni, R., and Park, Y.: MODIS Collection 6 (C6) LAI/FPAR Product User's Guide. 2015.

41. Myneni, R., and Knyazikhin, Y.: VIIRS/NPP Leaf Area Index/FPAR 8-Day L4 Global 500m SIN Grid V001., NASA EOSDIS Land Processes Distributed Active Archive Center, 2018.

42. Myneni, R. B., Hoffman, S., Knyazikhin, Y., Privette, J., Glassy, J., Tian, Y., Wang, Y., Song, X., Zhang, Y., and Smith, G.: Global products of vegetation leaf area and fraction absorbed PAR from year one of MODIS data, Remote sensing of environment, 83, 214-231, https://doi.org/10.1016/S0034-4257(02)00074-3, 2002.

43. Myneni, R. B., Yang, W., Nemani, R. R., Huete, A. R., Dickinson, R. E., Knyazikhin, Y., Didan, K., Fu, R., Juárez, R. I. N., and Saatchi, S. S.: Large seasonal swings in leaf area of Amazon rainforests, Proceedings of the National Academy of Sciences, 104, 4820-4823, https://doi.org/10.1073/pnas.0611338104, 2007.

44. Oliver, M. A., and Webster, R.: Kriging: a method of interpolation for geographical information systems, International Journal of Geographical Information System, 4, 313-332, https://doi.org/10.1080/02693799008941549, 1990.

45. Park, T., Yan, K., Chen, C., Xu, B., Knyazikhin, Y., and Myneni, R.: VIIRS Leaf Area Index (LAI) and Fraction of Photosynthetically Active Radiation Absorbed by Vegetation (FPAR) Product Algorithm Theoretical Basis Document (ATBD), NASA Technical Report, 2017.

46. Piao, S., Yin, G., Tan, J., Cheng, L., Huang, M., Li, Y., Liu, R., Mao, J., Myneni, R. B., and Peng, S.: Detection and attribution of vegetation greening trend in China over the last 30 years, Global change biology, 21, 1601-1609, https://doi.org/10.1111/gcb.12795, 2015.

47. Pu, J., Yan, K., Zhou, G., Lei, Y., Zhu, Y., Guo, D., Li, H., Xu, L., Knyazikhin, Y., and Myneni, R. B.: Evaluation of the MODIS LAI/FPAR Algorithm Based on 3D-RTM Simulations: A Case Study of Grassland, Remote Sensing, 12, 3391, https://doi.org/10.3390/rs12203391, 2020.

48. Pu, J., Roy, S., Knyazikhin, Y., and Myneni, R.: Sensor-Independent LAI/FPAR CDR. Zenodo [data set], https://doi.org/10.5281/zenodo.8076540, 2023a.

49. Pu, J., Yan, K., Gao, S., Zhang, Y., Park, T., Sun, X., Weiss, M., Knyazikhin, Y., and Myneni, R. B.: Improving the MODIS LAI compositing using prior time-series information, Remote Sensing of Environment, 287, 113493, https://doi.org/10.1016/j.rse.2023.113493, 2023b.

50. Roerink, G. J., Menenti, M., and Verhoef, W.: Reconstructing cloudfree NDVI composites using Fourier analysis of time series, International Journal of Remote Sensing, 21, 1911-1917, https://doi.org/10.1080/014311600209814, 2000.

51. Samanta, A., Ganguly, S., Vermote, E., Nemani, R. R., and Myneni, R. B.: Interpretation of variations in MODIS-measured greenness levels of Amazon forests during 2000 to 2009, Environmental Research Letters, 7, 024018, https://doi.org/10.1088/1748-9326/7/2/024018, 2012a.

52. Samanta, A., Knyazikhin, Y., Xu, L., Dickinson, R. E., Fu, R., Costa, M. H., Saatchi, S. S., Nemani, R. R., and Myneni, R. B.: Seasonal changes in leaf area of Amazon forests from leaf flushing and abscission, Journal of Geophysical Research: Biogeosciences, 117, https://doi.org/10.1029/2011JG001818, 2012b.

53. Sellers, P., Dickinson, R. E., Randall, D., Betts, A., Hall, F., Berry, J., Collatz, G., Denning, A., Mooney, H., and Nobre, C.: Modeling the exchanges of energy, water, and carbon between continents and the atmosphere, Science, 275, 502-509, https://doi.org/10.1126/science.275.5299.502, 1997.

54. Skidmore, A. K., Pettorelli, N., Coops, N. C., Geller, G. N., Hansen, M., Lucas, R., Mücher, C. A., O'Connor, B., Paganini, M., Pereira, H. M., Schaepman, M. E., Turner, W., Wang, T., and Wegmann, M.: Environmental science: Agree on biodiversity metrics to track from space, Nature, 523, 403-405, 10.1038/523403a, 2015.

55. Smith, P. R.: Bilinear interpolation of digital images, Ultramicroscopy, 6, 201-204, https://doi.org/10.1016/0304-3991(81)90061-9, 1981.

56. Sulla-Menashe, D., and Friedl, M. A.: User Guide to Collection 6 MODIS Land Cover (MCD12Q1 and MCD12C1) Product, http://girps.net/wp-content/uploads/2019/03/MCD12_User_Guide_V6.pdf, 2018.

57. Sun, Y., Knyazikhin, Y., She, X., Ni, X., Chen, C., Ren, H., and Myneni, R. B.: Seasonal and long-term variations in leaf area of Congolese rainforest, Remote Sensing of Environment, 268, 112762, https://doi.org/10.1016/j.rse.2021.112762, 2022.

58. Tang, X., Wang, Z., Xie, J., Liu, D., Desai, A. R., Jia, M., Dong, Z., Liu, X., and Liu, B.: Monitoring the seasonal and interannual variation of the carbon sequestration in a temperate deciduous forest with MODIS time series data, Forest ecology and management, 306, 150-160, https://doi.org/10.1016/j.foreco.2013.06.032, 2013.

59. Tian, Y., Zhang, Y., Knyazikhin, Y., Myneni, R. B., Glassy, J. M., Dedieu, G., and Running, S. W.: Prototyping of MODIS LAI and FPAR algorithm with LASUR and LANDSAT data, IEEE Transactions on geoscience and remote sensing, 38, 2387-2401, https://doi.org/10.1109/36.868894, 2000.

60. Wang, J., Yan, K., Gao, S., Pu, J., Liu, J., Park, T., Bi, J., Maeda, E. E., Heiskanen, J., and Knyazikhin, Y.: Improving the Quality of MODIS LAI Products by Exploiting Spatiotemporal Correlation Information, IEEE Transactions on Geoscience and Remote Sensing, 61, https://doi.org/10.1109/TGRS.2023.3264280, 2023.

61. Weiss, M., Baret, F., Garrigues, S., and Lacaze, R.: LAI and fAPAR CYCLOPES global products derived from VEGETATION. Part 2: validation and comparison with MODIS collection 4 products, Remote Sensing of Environment, 110, 317-331, https://doi.org/10.1016/j.rse.2007.03.001, 2007.

62. Whitt, M. W., and Ulaby, F. T.: Radar response of periodic vegetation canopies, International Journal of Remote Sensing, 15, 1813-1848, https://doi.org/10.1080/01431169408954211, 1994.

63. Xiao, Z., Liang, S., Wang, J., Chen, P., Yin, X., Zhang, L., and Song, J.: Use of General Regression Neural Networks for Generating the GLASS Leaf Area Index Product From Time-Series MODIS Surface Reflectance, IEEE Transactions on Geoscience and Remote Sensing, 52, 209-223, https://doi.org/10.1109/TGRS.2013.2237780, 2014.

64. Xu, B., Park, T., Yan, K., Chen, C., Zeng, Y., Song, W., Yin, G., Li, J., Liu, Q., Knyazikhin, Y., and Myneni, R.: Analysis of Global LAI/FPAR Products from VIIRS and MODIS Sensors for Spatio-Temporal Consistency and Uncertainty from 2012–2016, Forests, 9, https://doi.org/10.3390/f9020073, 2018.

65. Xu, B., Li, J., Park, T., Liu, Q., Zeng, Y., Yin, G., Yan, K., Chen, C., Zhao, J., and Fan, W.: Improving leaf area index retrieval over heterogeneous surface mixed with water, Remote Sensing of Environment, 240, 111700, https://doi.org/10.1016/j.rse.2020.111700, 2020.

66. Xu, L., Li, B., Yuan, Y., Gao, X., and Zhang, T.: A temporal-spatial iteration method to reconstruct NDVI time series datasets, Remote Sensing, 7, 8906-8924, https://doi.org/10.3390/rs70708906, 2015.

67. Yan, K., Park, T., Yan, G., Chen, C., Yang, B., Liu, Z., Nemani, R., Knyazikhin, Y., and Myneni, R.: Evaluation of MODIS LAI/FPAR Product Collection 6. Part 1: Consistency and Improvements, Remote Sensing, 8, https://doi.org/10.3390/rs8050359, 2016.

68. Yan, K., Park, T., Chen, C., Xu, B., Song, W., Yang, B., Zeng, Y., Liu, Z., Yan, G., and Knyazikhin, Y.: Generating global products of lai and fpar from snpp-viirs data: Theoretical background and implementation, IEEE Transactions on Geoscience Remote Sensing, 56, 2119-2137, https://doi.org/10.1109/TGRS.2017.2775247, 2018.

69. Yan, K., Pu, J., Park, T., Xu, B., Zeng, Y., Yan, G., Weiss, M., Knyazikhin, Y., and Myneni, R. B.: Performance stability of the MODIS and VIIRS LAI algorithms inferred from analysis of long time series of products, Remote Sensing of Environment, 260, 112438, https://doi.org/10.1016/j.rse.2021.112438, 2021a.

70. Yan, K., Zhang, Y., Tong, Y., Zeng, Y., Pu, J., Gao, S., Li, L., Mu, X., Yan, G., and Rautiainen, M.: Modeling the radiation regime of a discontinuous canopy based on the stochastic radiative transport theory: Modification, evaluation and validation, Remote Sensing of Environment, 267, 112728, https://doi.org/10.1016/j.rse.2021.112728, 2021b.

71. Yan, K., Zou, D., Yan, G., Fang, H., Weiss, M., Rautiainen, M., Knyazikhin, Y., and Myneni, R. B.: A Bibliometric Visualization Review of the MODIS LAI/FPAR Products from 1995 to 2020, Journal of Remote Sensing, 2021, https://doi.org/10.34133/2021/7410921, 2021c.

72. Yang, W., Tan, B., Huang, D., Rautiainen, M., Shabanov, N. V., Wang, Y., Privette, J. L., Huemmrich, K. F., Fensholt, R., and Sandholt, I.: MODIS leaf area index products: From validation to algorithm improvement, IEEE Transactions on Geoscience and Remote Sensing, 44, 1885-1898, https://doi.org/10.1109/TGRS.2006.871215, 2006.

73. Zhang, H., Liu, L., He, W., and Zhang, L.: Hyperspectral image denoising with total variation regularization and nonlocal low-rank tensor decomposition, IEEE Transactions on Geoscience and Remote Sensing, 58, 3071-3084, https://doi.org/10.1109/TGRS.2019.2947333, 2019.

74. Zhang, Y., Song, C., Band, L. E., Sun, G., and Li, J.: Reanalysis of global terrestrial vegetation trends from MODIS products: Browning or greening?, Remote Sensing of Environment, 191, 145-155, https://doi.org/10.1016/j.rse.2016.12.018, 2017.

75. Zheng, Y.-B., Huang, T.-Z., Zhao, X.-L., Jiang, T.-X., Ma, T.-H., and Ji, T.-Y.: Mixed noise removal in hyperspectral image via low-fibered-rank regularization, IEEE Transactions on Geoscience and Remote Sensing, 58, 734-749, https://doi.org/10.1109/TGRS.2019.2940534, 2019.

76. Zhou, J., Jia, L., and Menenti, M.: Reconstruction of global MODIS NDVI time series: Performance of Harmonic ANalysis of Time Series (HANTS), Remote Sensing of Environment, 163, 217-228, https://doi.org/10.1016/j.rse.2015.03.018, 2015.

710 77. Zhu, W., Pan, Y., He, H., Wang, L., Mou, M., and Liu, J.: A changing-weight filter method for reconstructing a high-quality NDVI time series to preserve the integrity of vegetation phenology, IEEE Transactions on Geoscience and Remote Sensing, 50, 1085-1094, https://doi.org/10.1109/TGRS.2011.2166965, 2011.

78. Zou, D., Yan, K., Pu, J., Gao, S., Li, W., Mu, X., Knyazikhin, Y., and Myneni, R. B.: Revisit the Performance of MODIS and VIIRS Leaf Area Index Products from the Perspective of Time-series Stability, IEEE Journal of Selected Topics in Applied Earth
715 Observations and Remote Sensing, https://doi.org/10.1109/JSTARS.2022.3214224, 2022.